NAVAL POSTGRADUATE SCHOOL

MONTEREY, CALIFORNIA

THESIS

HIGH ENERGY LASER PROPAGATION IN VARIOUS ATMOSPHERIC CONDITIONS UTILIZING A NEW, ACCELERATED SCALING CODE

by

Chris R. Fussman

June 2014

Thesis Advisor: Keith R. Cohn
Co-Advisor: William B. Colson

Approved for public release; distribution is unlimited

THIS PAGE INTENTIONALLY LEFT BLANK

REPORT DOCUMENTATION PAGE		Form Approved OMB No. 0704–0188

1. AGENCY USE ONLY *(Leave blank)*	2. REPORT DATE June 2014	3. REPORT TYPE AND DATES COVERED Master's Thesis

4. TITLE AND SUBTITLE
HIGH ENERGY LASER PROPAGATION IN VARIOUS ATMOSPHERIC CONDITIONS UTILIZING A NEW, ACCELERATED SCALING CODE

5. FUNDING NUMBERS

6. AUTHOR(S) Chris R. Fussman

7. PERFORMING ORGANIZATION NAME(S) AND ADDRESS(ES)
Naval Postgraduate School
Monterey, CA 93943–5000

8. PERFORMING ORGANIZATION REPORT NUMBER

9. SPONSORING /MONITORING AGENCY NAME(S) AND ADDRESS(ES)
N/A

10. SPONSORING/MONITORING AGENCY REPORT NUMBER

11. SUPPLEMENTARY NOTES The views expressed in this thesis are those of the author and do not reflect the official policy or position of the Department of Defense or the U.S. Government. IRB Protocol number ____N/A____.

12a. DISTRIBUTION / AVAILABILITY STATEMENT Approved for public release; distribution is unlimited	**12b. DISTRIBUTION CODE** A

13. ABSTRACT (maximum 200 words)

For this thesis, an atmospheric propagation code named ANCHOR (Atmospheric NPS Code for High Energy Laser Optical pRopagation) was developed and utilized to study the propagation of high energy lasers in various atmospheric conditions and for numerous laser configurations. The ANCHOR code accesses existing industry databases to obtain relevant optical properties for various atmospheres and then uses scaling laws to simulate laser propagation through the defined environments.

ANCHOR accounts for the effects of atmospheric diffraction, turbulence, platform jitter and thermal blooming on the laser beam, and outputs on-target irradiance and power-in-the-bucket profiles for a wide range of laser wavelengths. Several known physical trends associated with laser propagation will be reproduced, and the results will be compared to the industry accepted propagation code Wavetrain.

The results of ANCHOR studies will indicate that the 100 kW-class high energy laser can effectively engage slow-moving targets at ranges greater than five kilometers in clear weather by delivering enough energy to melt 0.1 liters of one millimeter-thick aluminum aircraft skin in five seconds. For hazy, turbulent, and rainy conditions, the laser can effectively engage targets from ranges closer than three kilometers, but reasonable dwell times are only achieved for ranges closer than two kilometers.

14. SUBJECT TERMS Directed energy weapons, high energy lasers, atmospheric propagation simulations, scaling codes	**15. NUMBER OF PAGES** 113
	16. PRICE CODE

17. SECURITY CLASSIFICATION OF REPORT Unclassified	**18. SECURITY CLASSIFICATION OF THIS PAGE** Unclassified	**19. SECURITY CLASSIFICATION OF ABSTRACT** Unclassified	**20. LIMITATION OF ABSTRACT** UU

NSN 7540–01–280–5500

Standard Form 298 (Rev. 2–89)
Prescribed by ANSI Std. 239–18

THIS PAGE INTENTIONALLY LEFT BLANK

HIGH ENERGY LASER PROPAGATION IN VARIOUS ATMOSPHERIC CONDITIONS UTILIZING A NEW, ACCELERATED SCALING CODE

Chris R. Fussman
Ensign, United States Navy
B.S., United States Naval Academy, 2013

Submitted in partial fulfillment of the
requirements for the degree of

MASTER OF SCIENCE IN APPLIED PHYSICS

from the

NAVAL POSTGRADUATE SCHOOL
June 2014

Author: Chris R. Fussman

Approved by: Keith R. Cohn
                 Thesis Advisor

                 William B. Colson
                 Co-Advisor

                 Andres Larraza,
                 Chair, Department of Physics

iii

THIS PAGE INTENTIONALLY LEFT BLANK

ABSTRACT

For this thesis, an atmospheric propagation code named ANCHOR (Atmospheric NPS Code for High Energy Laser Optical pRopagation) was developed and utilized to study the propagation of high energy lasers in various atmospheric conditions and for numerous laser configurations. The ANCHOR code accesses existing industry databases to obtain relevant optical properties for various atmospheres and then uses scaling laws to simulate laser propagation through the defined environments.

ANCHOR accounts for the effects of atmospheric diffraction, turbulence, platform jitter and thermal blooming on the laser beam, and outputs on-target irradiance and power-in-the-bucket profiles for a wide range of laser wavelengths. Several known physical trends associated with laser propagation will be reproduced, and the results will be compared to the industry accepted propagation code Wavetrain.

The results of ANCHOR studies will indicate that the 100 kW-class high energy laser can effectively engage slow-moving targets at ranges greater than five kilometers in clear weather by delivering enough energy to melt 0.1 liters of one millimeter-thick aluminum aircraft skin in five seconds. For hazy, turbulent, and rainy conditions, the laser can effectively engage targets from ranges closer than three kilometers, but reasonable dwell times are only achieved for ranges closer than two kilometers.

THIS PAGE INTENTIONALLY LEFT BLANK

TABLE OF CONTENTS

THIS PAGE INTENTIONALLY LEFT BLANK

LIST OF FIGURES

LIST OF TABLES

THIS PAGE INTENTIONALLY LEFT BLANK

LIST OF ACRONYMS AND ABBREVIATIONS

HEL	high-energy laser
DE	directed energy
ABL	airborne laser system
COIL	chemical oxygen iodine laser
DOD	Department of Defense
FEL	free-electron laser
HITRAN	high-resolution transmission
LAWS	laser weapon system
LBLRTM	line-by-line radiative transfer model
LCS	littoral combat ship
MIRACL	mid-infrared advanced chemical laser
MLD	maritime laser demonstrator
MODTRAN	moderate resolution atmospheric transmission
PRF	pulse repetition frequency
SAM	surface-to-air missile
SSL	solid-state laser
STP	standard temperature and pressure
LEEDR	laser environmental effects definition and reference
AFIT	Air Force Institute of Technology

THIS PAGE INTENTIONALLY LEFT BLANK

ACKNOWLEDGMENTS

THIS PAGE INTENTIONALLY LEFT BLANK

I.   INTRODUCTION

The United States Navy is heavily invested in the research and development of high-energy lasers (HELs) onboard various surface and air platforms for offensive and defensive capabilities [1], [2]. Such weapons, while extremely complex in design and expensive to manufacture, hold many advantages to currently-employed conventional weapons systems. From speed-of-light payload delivery, to an extremely deep magazine, to engagement flexibility for soft and hard kills, laser weapons are often touted as a significant part of the future of naval warfighting [3].

Unlike conventional weapons, however, laser weapons are uniquely affected by weather conditions of the environment in which they are employed [4]. Effective development of these weapons is closely tied to the proper modeling and understanding of the role that atmospheric properties play in hindering or aiding laser propagation. Unfortunately, simply relying on experimental studies in order to fully parameterize laser behavior in various weather conditions is neither time-efficient nor cost-effective [4]. Physics-based computer modeling is therefore essential to guide HEL-based research.

To this end, a streamlined and robust simulation code has been developed by the NPS Directed Energy Group. The code utilizes existing atmospheric databases and governing scaling equations to accurately and efficiently model laser propagation in various environments for numerous laser configurations. The code has been used to explore atmospheres with variable turbulence profiles, visibilities and precipitation, as well as laser effectiveness with various beam diameters, output powers, wavelengths, etc.

The first part of this thesis will discuss the history, technology and advantages of directed energy weapons. Next, the thesis will explore the physical principles of atmospheric propagation, followed by atmospheric modeling, and then the simulation methods utilized to carry out the laser propagation studies. Lastly, the thesis results will be discussed and analyzed, with conclusions tying together the quantitative and qualitative aspects of the research.

THIS PAGE INTENTIONALLY LEFT BLANK

II.   DIRECTED ENERGY WEAPON OVERVIEW

A.   DIRECTED ENERGY INTRODUCTION

A directed energy (DE) weapon emits energy directed at a target in order to inflict damage without the use of a projectile [5]. The energy harnessed by a DE weapon is usually in the form of electromagnetic radiation, which includes microwave weapons and lasers, but also can include particle-beams and sonic weapons. Currently, DE weapons of military interest utilize a laser (light amplification by stimulated emission of radiation) to generate and deliver a concentrated spot of light at a specific wavelength and of high enough irradiance on the surface of a target to cause damage. The wavelength range of the laser light typically lies in the visible to infrared regime (~0.5 μm to 20 μm), and the energy propagates as a narrow beam at the speed of light to reach the target. Damage is primarily inflicted by the high-energy laser "by light dwelling on the target for an extended period of time to accumulate deposited energy and inflict thermal damage" [4].

Laser lethality, defined as "the capability of a weapon system to render a target non-functional," [4] greatly depends on the target material the amount of power transmitted to the target. Thermal damage is considered to be the main lethality mechanism for lasers, resulting in the burning, melting, penetration or structural integrity failure of the target [4]. For typical targets, such as the carbon-carbon ceramic nosecone of a surface-to-air missile (SAM), an estimated 12.1 kilowatts (kW) of power over a dwell time of 4 seconds is required to ablate a depth of 1.0 cm on the target [6]. While a laser emitting such an output power level may not appear to be powerful enough to neutralize a missile traveling at Mach 3.0, a DE weapon of three-times the power and dwell time of the example may very well cause enough structural damage to "bring about catastrophic aerodynamic instability which would tear the missile apart" [6].

The first laser, constructed by Theodore H. Maiman in 1960, was a pulsed ruby laser with approximately one watt of output power [4]. Almost immediately following this initial invention, the U.S. Department of Defense (DOD) heavily invested into the research and development of lasers as operational military weapons systems. Several

military entities have since developed multiple HEL weapons systems for operational deployment. The U.S. Air Force has constructed the Advanced Tactical Laser and the Airborne Laser (ABL) test-bed, both of which employ aircraft-mounted systems utilizing chemical oxygen iodine lasers (COILs) with output powers of 100 kW and one megawatt (MW), respectively [4].

The U.S. Navy has also developed several sophisticated weapons platforms, including the Mid-Infrared Advanced Chemical Laser (MIRACL), the Laser Weapon System (LAWS), and the Maritime Laser Demonstrator (MLD). The MIRACL system, first made operational in 1980, employs a deuterium-fluoride laser with ~one MW output power, while LAWS and MLD employ a solid-state fiber laser and a solid-state slab laser with output power of 32 kW and ~100 kW, respectively [4]. The latter laser system, the MLD, also became the first to be tested on and powered by a ship in 2011 onboard the U.S. Navy defense test ship USS *Paul Foster* (DD-964). The most significant achievement in the implementation of a DE weapon system onboard a naval platform, however, is the slated operational deployment of the aforementioned LAWS on the USS *Ponce* (LPD-15) in the Persian Gulf during summer 2014 [7].

B.   ADVANTAGES OF HELS

Conceptually, directed energy weapons systems have significant superiority to most conventional weapons systems. The main advantages of DE weapons lie in the precision and speed of payload delivery, low cost per engagement, and an essentially unlimited magazine [4]. A laser is capable of focusing to a spot several centimeters in diameter on a target from a range of up to 10 km [6]. Unlike most conventional weapons, such as explosive missiles and kinetic rounds, DE weapon precision also greatly reduces the possibility of collateral damage. Furthermore, due to the speed of light delivery of damage, a directed energy weapon has the potential of engaging and destroying a target soon after it is detected, whereas munitions from a conventional weapon must travel toward the target at a much slower rate and thus engage it at a close range. Radar may also be utilized for multi-target tracking, allowing for the continuous adjustment of the

HEL to maintain the beam on a single target while predicting the future location of any other targets for subsequent engagement.

DE weapons systems are comprised of all-electric components, and complete integration into a naval ship's power grid provides for a magazine potentially limited only by the ship's power. All-electric DE weapons are thus by design a relatively cost-effective platform, and several second "shots" from an HEL are only theoretically tied to the price per gallon of the platform's fuel. Although the initial overhead cost of DE weapon design and implementation has caused significant postponement in a budget-constrained environment, the cost per shot compared to an advanced tactical missile makes the HEL a worthy long-term investment.

C.   HEL TECHNOLOGY

The primary types of DE weapons the U.S. Navy is considering for employment on expeditionary naval platforms are solid-state lasers (SSLs) and free-electron lasers (FELs) [1]. Regardless of specific platform, the ideal HEL weapon system should exhibit several design traits. The system should have high wall-plug efficiency to generate the most optical power with as little input power as possible. The HEL should utilize a gain medium with high thermal conductivity for rapid heat removal from the system. The lasing medium should also be resilient against heat and/or dielectric breakdown to allow for scaling to higher power without permanent damage to the weapon. Finally, the output optical wavelength should reside in a region of atmospheric transparency, so as to minimize the amount of attenuation of the laser energy and to maximize the amount of energy delivered to the target.

1.   Solid-State Lasers

SSL technology utilizes a solid substrate that holds the dopant in which the lasing transitions occur. Because this technology utilizes a material medium, substrate damage threshold limits output power [4]. SSLs have several advantages over FELs, including their relatively compact and lightweight design (for low or modest power outputs), relative power efficiency, and relative operational safety in the absence of potential stray radiation. Most importantly, SSLs are more technically mature than FELs, and can

potentially see more near term deployment availability. However, SSLs also have several disadvantages to FELs, including the lack of scalability to MW-class, a fixed optical wavelength primarily determined by the gain medium, and difficulty in obtaining acceptable beam quality for high-energy applications [1], [4]. Furthermore, DE applications require the combination of multiple solid-state lasers to attain the necessary power output to inflict damage on target, which increases their size and weight and degrades beam quality.

The two types of SSLs which have been employed as tactical weapons by the DOD are slab lasers and fiber lasers [1]. A slab laser couples pump light with laser energy through one side of a rectangular medium slab, while removing heat from the opposite side of the slab. A fiber laser, on the other hand, utilizes a long, thin, cylindrical rod medium, covered by cladding, to couple light to. While slab lasers have the geometrical advantage of a larger aspect ratio which allows for more light coupling (as output power is proportional to aspect ratio), fiber lasers are more lightweight, power efficient, durable and have comparable output power to slab lasers with potentially better beam quality in a smaller device.

Furthermore, optical waveguides in fiber lasers span many meters in length, providing a much larger surface area that allows for easier cooling than a slab laser. While such advantages indicate that the fiber SSL is a theoretically superior technology to the slab SSL, the latter has actually demonstrated higher output power with the ~105 kW of the MLD, as opposed to the ~33 kW fiber SSL LAWS [1]. Ultimately, however, the most significant issue with SSLs, which the FEL may be able to address, lies in the difficulty of coherent beam shaping from combining multiple SSLs, which is necessary to attain higher output power [4].

2.   Free-Electron Lasers

Free-electron lasers utilize free (unbound) electrons to generate light [4]. An electron gun, consisting of an electron-generating cathode and an accelerator, creates the initial electron beam. While several types of cathodes can be employed to generate electron beams, thermionic, or "hot" cathodes are preferred for FEL applications due to

their much higher power density [4]. The electrons are accelerated to relativistic speeds within a linear accelerator, and subsequently pass through an undulator, consisting of a series of magnets which generate an alternating magnetic field, causing the electrons to "wiggle" and emit light. The interaction of the electrons with the light in the resonator produces stimulated, coherent emission. The wavelength of the light produced depends on the energy of the electrons and the properties of the undulator. Furthermore, wall-plug efficiency of the system can be increased by recovering most of the energy of spent electrons [4].

Because FELs utilize free electrons as the gain medium, elimination of waste heat is not an issue and thus their output power is thought to be scalable to megawatt class. Furthermore, the FEL optical wavelength is tunable, and thus can be chosen for optimal atmospheric transparency. An FEL can also obtain excellent beam quality at high output power for long-distance propagation and a relatively energy-efficient design. However, FELs tend to be rather large in size (~ 20 meters long), heavy, and expensive to design [1]. FELs also require shielding to contain radiation produced by stray electrons, and the overall technology is relatively less mature compared to SSLs.

D.   HEL MISSIONS AND PLATFORMS

The missions of a DE weapon are largely dependent on its output power level. Directed energy weapons with lower power output (10–100 kW), such as the SSL, are better suited against slower moving targets, such as small watercraft and aircraft. Such DE weapons could immobilize boats and down aerial drones, as well as offer the potential of "soft kills" by blinding incoming missiles. Megawatt-class DE weapons, such as the FEL, will be primarily slated for cruise missile defense. The current FEL DOD project, the Innovative Naval Prototype, maintains a planned 100 kW of output power and is a stepping stone in the future transition to the MW-class devices.

The HEL weapons systems of both kW and MW-class could be fittingly employed on several naval platforms, such as the future all-electric ships, littoral combat ships (LCS), guided-missile destroyers (DDG-51 and DDG-1000), and the future Ford class aircraft carriers, such as the *Gerard R. Ford* (CVN-78). Due to weight and size

constraints, only SSLs could be potentially employed on Naval aviation platforms such as F/A-18E/F Hornet, F-35 Joint Strike Fighter (JSF) [8], and Marine Corps helicopter platforms such as the UH-1Y Huey and AH-1Z Cobra [6].

III. ATMOSPHERIC PROPAGATION OVERVIEW

The effectiveness of HEL weapons systems can be greatly affected by the medium through which the laser energy propagates. Because this medium is the Earth's atmosphere, one needs to understand the various optical properties and physical principles associated with this environment to be able to develop systems that can operate effectively within it.

A. ATMOSPHERIC EXTINCTION

Molecules and aerosols suspended in the atmosphere absorb and scatter propagating laser energy as it travels to reach the target [4]. Absorption occurs when photons from incident radiation (such as laser light) transfer their energy to atmospheric constituents, thereby heating the local atmosphere. Scattering occurs when incident photons are redirected from the beam in random directions by atmospheric particulates.

These combined effects are illustrated by Beer's Law in Equation (1), which describes the transmission of light through a linear medium, following

$$P(z) = P_0 e^{-\epsilon z}. \tag{1}$$

In Equation (1), P represents the total power delivered to a plane located a distance z from the source and P_0 is the initial output power at the beam director. The variable ϵ represents the total extinction coefficient due to atmospheric absorption and scattering (in units of inverse length), and is further described by Equation (2) as

$$\epsilon = \alpha_m + \alpha_a + \beta_m + \beta_a. \tag{2}$$

In Equation (2), α refers to the absorption coefficients and β refers to the scattering coefficients, while subscripts m and a denote the molecular and aerosol contributions, respectively. An increase in ϵ results in greater attenuation rate of laser light by the atmosphere.

1. Molecular Effects

Table 1 displays a list of the major molecular constituents which make up the Earth's atmosphere.

The Composition of the Atmosphere[a]			
Permanent constituents		**Variable constituents**	
Constituent	% by volume	Constituent	% by volume
Nitrogen (N_2)	78.084	Water vapor (H_2O)	0–0.04
Oxygen (O_2)	20.948	Ozone (O_3)	0–12×10^{-4}
Argon (Ar)	0.934	Sulfur dioxide (SO_2)[b]	0.001×10^{-4}
Carbon dioxide (CO_2)	0.036	Nitrogen dioxide (NO_2)[b]	0.001×10^{-4}
Neon (Ne)	18.18×10^{-4}	Ammonia (NH_3)[b]	0.004×10^{-4}
Helium (He)	5.24×10^{-4}	Nitric oxide (NO)[b]	0.0005×10^{-4}
Krypton (Kr)	1.14×10^{-4}	Hydrogen sulfide (H_2S)[b]	0.00005×10^{-4}
Xenon (Xe)	0.089×10^{-4}	Nitric acid vapor (HNO_3)	Trace
Hydrogen (H_2)	0.5×10^{-4}	Chlorofluorocarbons	Trace
Methane (CH_4)	1.7×10^{-4}	($CFCl_3$, CF_2Cl_2	
Nitrous oxide (N_2O)[b]	0.3×10^{-4}	CH_3CCl_3, CCl_4, etc.)	
Carbon monoxide (CO)[b]	0.08×10^{-4}		

[a] After the U.S. Standard Atmosphere (1976) with modifications.
[b] Concentration near the earth's surface.

Table 1. Molecular composition of Earth's atmosphere. From [9].

Ambient air is predominately composed of N_2 and O_2, both of which are linear, homonuclear molecules with symmetric molecular bonds between each of their two atoms. Because these molecules only possess one normal vibrational mode that does not alter their overall dipole moments, propagating optical energy does not cause these molecules to vibrate. Thus, N_2 and O_2 also do not absorb electromagnetic radiation in the infrared spectral region [9].

Instead, other atmospheric constituents, such as H_2O vapor and CO_2, dominate the infrared atmospheric absorption spectrum. Even though these molecules contribute to a very small percentage of the total atmospheric composition, they are asymmetrically-shaped and exhibit multiple vibrational modes, making them strong absorbers of electromagnetic radiation [9]. The molecular absorption is extremely intricate and ideal laser performance requires that the spectral width of the beam fits within a wavelength window containing minimum absorption features. A typical molecular absorption spectrum for a wavelength range of 0.5 μm to 5.0 μm is shown in Figure 1. The gaps in the data at ranges ∼2.5 to 3 μm, ∼4.25 to 4.5 μm and ∼4.75 to 5.0 μm are due to the absorption coefficient nearing infinity, which represents wavelength ranges of high absorption.
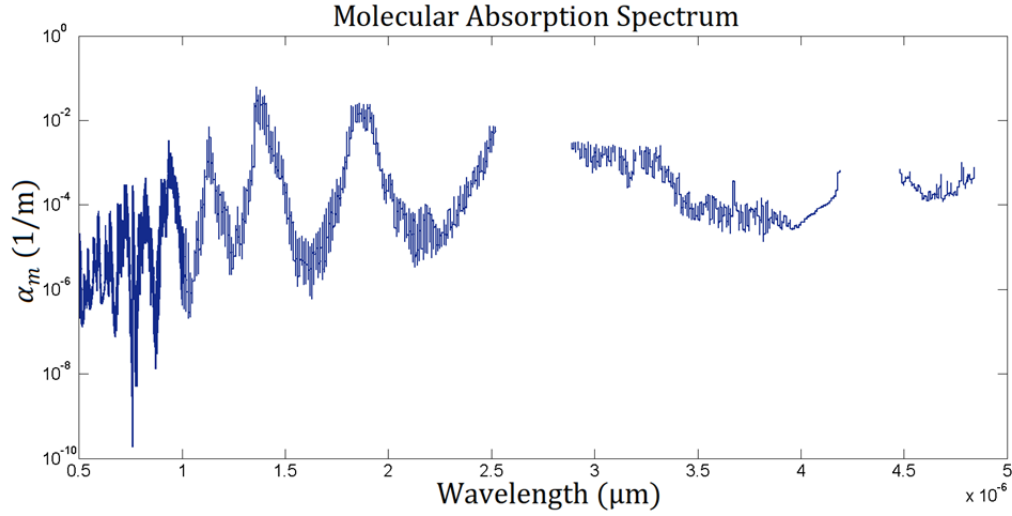
Figure 1. Typical molecular absorption spectrum for the atmosphere. Gaps in the data correspond to high molecular absorption coefficient α_m.

Figure 2 displays a typical molecular scattering spectrum for the atmosphere over a wavelength range of 0.5 µm to 5.0 µm. Molecular scattering is described by an optical phenomenon known as Rayleigh scattering, in which shorter wavelengths of electromagnetic energy are scattered more readily than longer wavelengths. Rayleigh scattering will be further discussed in Chapter IV, Section B.4.
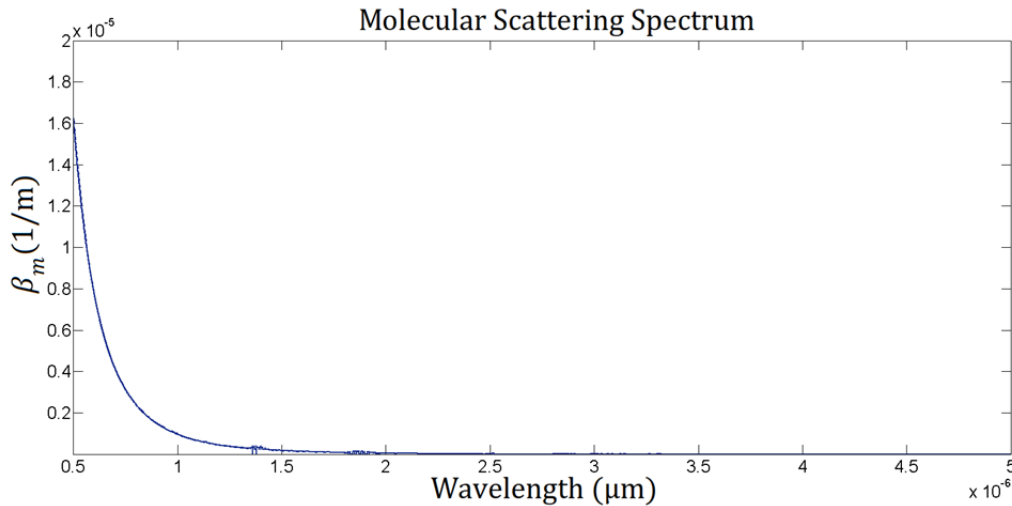
Figure 2. Typical molecular scattering spectrum for the atmosphere. As a result of Rayleigh scattering (discussed in Chapter IV), shorter wavelengths of light scatter more readily than longer wavelengths.

Most of the photons scattered by molecules have the same wavelength as the incident photons; only their direction of propagation changes. This principle readily describes the phenomenon of the blue daytime sky and red sunsets. Because blue light more readily undergoes molecular scattering than red light, the daytime sky appears blue [9]. At sunset, the path length of light from the setting sun to the viewer through the atmosphere is longer, and by the time the light reaches the viewer's eyes most of the shorter wavelength light has been scattered, leaving only the longer wavelength red light [9].

2. Aerosol Effects

Absorption and scattering effects on light by aerosols are similar in nature to those by molecules. However, the extent of these effects depends greatly on aerosol size, shape and refractive index, the latter primarily defined by the material properties of the individual particles (water, dust, etc.). Figure 3 displays a plot of the aerosol absorption spectrum, while Figure 4 displays a plot of the aerosol scattering spectrum, both for a 0.5 μm to 5.0 μm wavelength range.
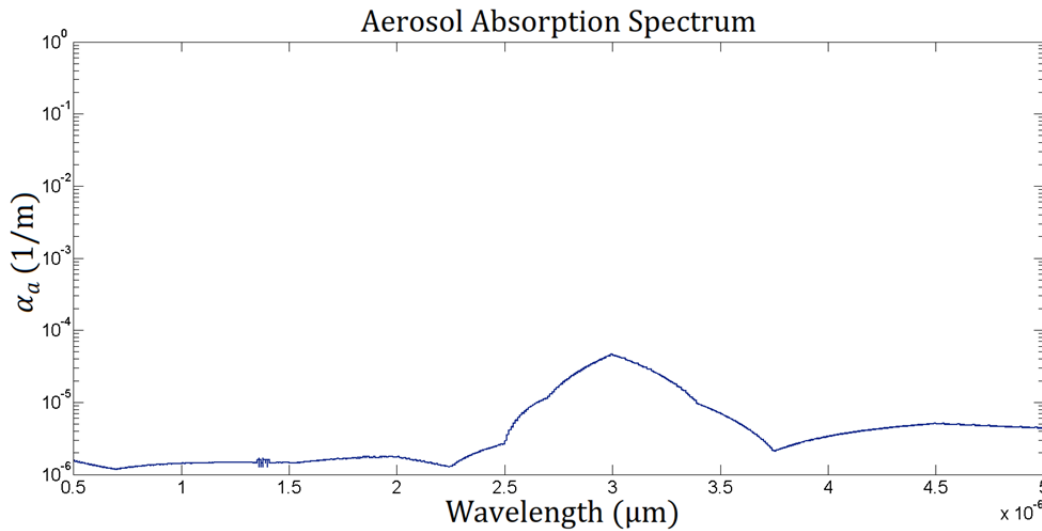
Figure 3. Typical aerosol absorption spectrum for the atmosphere. The peak in aerosol absorption at ~3 μm corresponds to presence of particulates which specifically absorb at those wavelengths.
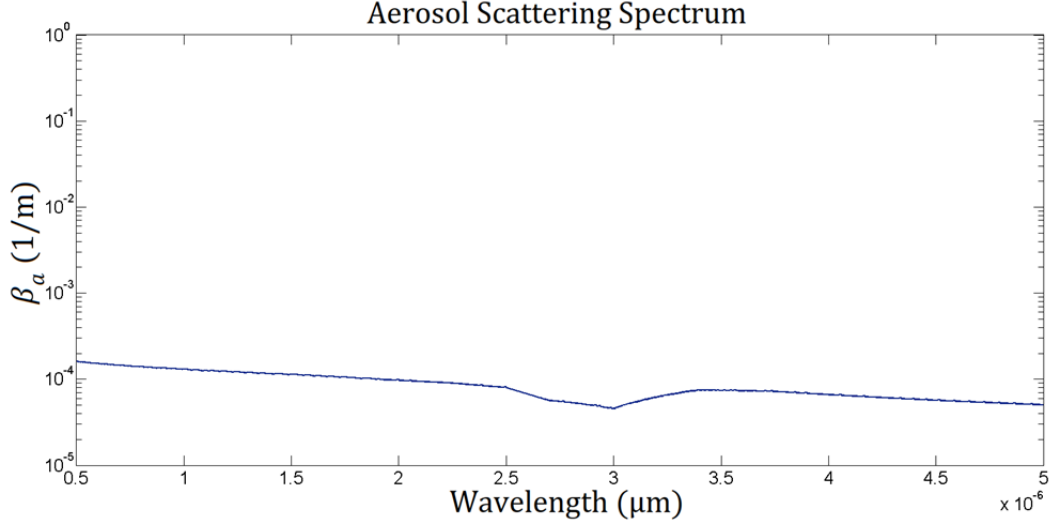
Figure 4.   Typical aerosol scattering spectrum for the atmosphere. Aerosols scatter most wavelengths relatively equally.

Because most aerosols are similar in size to the wavelength of infrared or visible light, they absorb most wavelengths approximately equally [5]. The notable increase in scattering at ~ 3 μm may be due to particulates such as sulfate (SO_2) or sea salt aerosols, which may absorb more at this specific wavelength because of their size.

Similarly, aerosol particulates also scatter most wavelengths in the infrared and visible range relatively equally, which explains why clouds and haze appear approximately white to the human eye [9].

B.   ATMOSPHERIC TURBULENCE

Turbulence is a term generally describing a fluid flow regime within a medium in which the flow exhibits an irregular, chaotic and dissipative pattern, mostly in the form of randomly-varying eddies [10]. In the atmosphere, the turbulent flow of air is considered to be small-scale and primarily the result of convective air motion, vertical temperature differences, and wind shear.

The major effects of turbulence on electromagnetic energy propagation stem from the spatial and temporal fluctuations in the refractive index of air [10]. The relationship between absolute temperature T (in K), wavelength λ (in μm), pressure P (in mbar) and the refractive index of air n can be described by [10]

13

$$n \approx 1 + 77.6 \times 10^{-6} \left[1 + 7.52 \times 10^{-3} \lambda^{-2} \right] \frac{P}{T}. \tag{3}$$

Sufficient turbulence in the local atmosphere leads to variations in the local ambient temperature, which in turn leads to variations in the refractive index. For HEL weapons systems to function most effectively, the propagation of laser energy through the atmosphere requires that the light rays emitted by the laser maintain transverse coherence so that they constructively interfere to form a high irradiance spot size on target. However, refractive index variations due to turbulence cause different parts of the laser beam to experience different path lengths as the beam propagates, which disrupts constructive interference at the target and can even cause the beam to spread out and/or scintillate (i.e., break up into beamlets) [10].

The Fried parameter r_0 (units of length) can be used to estimate the effects of turbulence on laser propagation. The r_0 parameter defines a circular diameter over which the laser beam maintains coherence (no significant change in phase) in the transverse direction throughout the propagation distance [4]. In other words, r_0 estimates the maximum transverse separation at the source between two individual light rays within which the two rays will constructively interfere at the target. A lower r_0 value implies stronger turbulence. If the r_0 value is significantly smaller than the beam director size, the laser beam will break up into many smaller, incoherently radiating beamlets.

The relationship between r_0, the refractive structure constant C_n^2, the wavelength of light λ, and the distance to target ℓ can be quantified by

$$r_0 \approx 0.33 \frac{\lambda^{6/5}}{\left(\ell^{3/5} C_n^2 \right)^{3/5}}. \tag{4}$$

For typical wavelength and target ranges for HEL applications, r_0 can range from $\sim$one centimeter in strong turbulence to 10's of centimeters in weak turbulence. The C_n^2 value (in units of m$^{-2/3}$) characterizes the strength of the turbulence. The C_n^2 value was first theoretically parameterized by Andrey Kolmogorov and has been measured at numerous

locations worldwide [4]. The significance of the C_n^2 value stems from Kolmogorov's original theory for turbulent flow, which has formed the basis for all contemporary turbulence theories [4].

The basic idea behind Kolmogorov's theory is this: Turbulent fluid flow is governed by the Navier-Stokes equations, but significant challenges lie in solving these equations within a system as expansive as the atmosphere. Kolmogorov's theory therefore utilizes a statistical approach in describing the flow of kinetic energy from large-scale eddies, which can be tens to hundreds of meters in size, into smaller eddies, which are typically millimeters to centimeters in size [10]. Eddies within this range of sizes, which is defined as the inertial subrange, are assumed to be relatively homogeneous and isotropic within smaller regions of space [4], and thus properties such as the refractive index vary over space and time in identically-distributed increments. This assumption allowed for Kolmogorov to utilize a structure function in describing turbulence, which is represented by the C_n^2 value.

In atmospheric modeling, an increase in the C_n^2 value yields an increase in the amount of atmospheric turbulence. Furthermore, the parameter tends to be a strong function of altitude, and generally decreases at higher altitudes. Weak atmospheric turbulence would exhibit a value of $C_n^2 \approx 10^{-17}\,\mathrm{m}^{-2/3}$, while strong turbulence would occur if $C_n^2 \approx 10^{-13}\,\mathrm{m}^{-2/3}$.

C.   THERMAL BLOOMING

Thermal blooming describes a non-linear phenomenon in which propagating laser light deposits a small portion of its energy along the beam path into the local atmosphere. As the laser energy is absorbed by the molecules and aerosols in the air, the ambient air temperature increases, creating localized gradients in air density, subsequently altering the refractive index of the medium [11] (see Equation 3). A sufficient change in the refractive index effectively creates a diverging, concave lens within the volume of the laser beam, which exhibits a greater lens thickness and thus optical density at the edges

than at the center [5]. Ultimately, this lens causes the beam to "bloom," or diverge from its propagation path, effectively reducing the irradiance on target.

1. Paraxial Wave Equation

The effects of thermal blooming on HEL beam propagation can be estimated by first assuming that the electric field of the propagating electromagnetic energy takes the form of

$$E(\mathbf{r}) = \psi(\mathbf{r})e^{ikz}, \tag{5}$$

where $\psi(\mathbf{r})$ is the slowly-varying complex envelope and the harmonic factor $e^{-i\omega t}$ has been suppressed. Here, $k = 2\pi / \lambda$ is the wave number, λ is the laser wavelength, z is the primary direction of propagation, and the real part of E specifies the electric field. The irradiance of the energy in SI units thus takes the form of

$$I(\mathbf{r}) = \frac{c\epsilon_0}{2} E^* E = \frac{c\epsilon_0}{2} \psi^* \psi, \tag{6}$$

where ψ^* represents the complex conjugate of wave function ψ. Equation (5) represents a solution to the paraxial wave equation, which follows as [11]

$$\frac{\partial \psi}{\partial z} = -\frac{\epsilon}{2}\psi + \frac{i}{2k}\nabla_{\perp}^2 \psi + (ik\delta n)\psi, \tag{7}$$

where $-\epsilon\psi/2$ represents atmospheric extinction (see section III A.), $i\nabla_{\perp}^2\psi/2k$ represents transverse diffraction, $\nabla_{\perp}^2 = \partial^2/\partial x^2 + \partial^2/\partial y^2$ is the transverse Laplace operator, and the $(ik\delta n)\psi$ component describes the effects of varying the refractive index δn due to thermal blooming (and in principle, turbulence).

As stated previously, a change in air temperature has a direct effect on the refractive index of the absorbing medium, described by

$$\delta n = \frac{dn}{dT}\Delta T = -\frac{n_0 - 1}{T_o}\Delta T, \tag{8}$$

where n_0 is the averaged refractive index of air, T_o is the ambient temperature, and ΔT represents the increase in temperature due to absorption.

16

For most HEL weapon systems, it is common to assume that the rate of heating is too small to create pressure differences (assumed to be nearly instantaneous) [11], resulting in constant-pressure, or isobaric, heating. The temperature rise due to laser heating under these conditions can be described using the energy balance equation, given by [11]

$$\frac{\partial \Delta T}{\partial t} = \frac{\alpha}{\rho C_p} I - \left(\mathbf{v} \cdot \nabla_\perp\right)\Delta T + \left(\frac{K}{\rho C_p}\nabla_\perp^2\right)\Delta T .$$ (9)

In Equation (9), the $\alpha I / \rho C_p$ term represents laser heating, where α is the atmospheric absorption coefficient, ρ is the air density, C_p is the constant-pressure specific heat, and I is the laser irradiance. The $\left(\mathbf{v} \cdot \nabla_\perp\right)\Delta T$ term represents the effects of energy exchange by convection, where $\mathbf{v}$ is the wind velocity, $\nabla_\perp$ is the transverse gradient operator. The $\left(K\nabla_\perp^2 / \rho C_p\right)\Delta T$ term represents conduction of heat through the air, where K is the thermal conductivity.

In most HEL propagation scenarios, convection dominates conduction except for conditions involving absolutely calm winds. If one assumes that the laser beam's pulse repetition frequency (PRF) remains low enough to allow the locally heated air to be removed from the beam path by either wind or beam motion, then the conduction term can essentially be ignored in what is defined as convection-dominated thermal blooming [11].

2.   Steady-State Phase Distortion without Wind

In the case of a stationary beam and no wind $\left(|\mathbf{v}| = 0\right)$, the thermal blooming due to absorption approaches the steady-state conduction-dominated scenario. The magnitude of conduction-dominated thermal blooming on the laser beam can be evaluated using the dimensionless scaling parameter given by [12]

$$D_C = -\frac{n_T P \alpha z^2}{2\pi K n_o a^2}, \quad \alpha z \ll 1,$$ (10)

where from Equation (8) we obtain that $n_T = dn/dT = -(n_o - T_o)/T_o$, P is the laser power, z is the distance that the beam has propagated through the absorbing medium, and a is the beam radius. The on-axis decrease in beam intensity due to conduction-dominated thermal blooming can be approximated by e^{-D_C} [11].

For the contribution of conduction to thermal blooming to be ignored, the wind speed $|\mathbf{v}|$ must satisfy the condition $|\mathbf{v}| \gg \chi/a$, where $\chi = K/\rho C_p$ represents the thermal diffusivity of the medium ($\chi \approx 0.2 \, \text{cm}^2/s$ for air at 300 K) [11]. Because the ratio of the thermal diffusivity to the beam radius is virtually negligible in comparison to wind speed for all scenarios but those involving absolutely no wind, this condition is nearly always satisfied for laser propagation.

3.   Steady-State Phase Distortion with Wind

Phase distortion due to thermal blooming in the presence of wind has a very specific effect on the laser beam irradiance on target, illustrated by Figure 5.
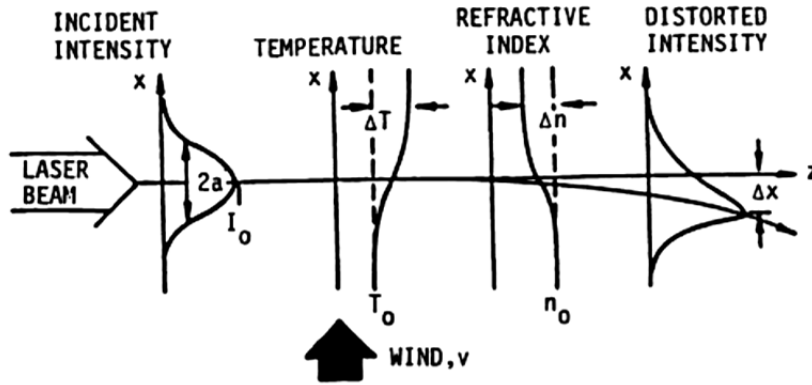
Figure 5.   The effects of steady-state thermal blooming with a transverse wind, from [11].

18

As the transverse wind component moves across the beam propagation path, it causes the local air temperature to increase in the downwind direction. As temperature change is inversely proportional to both the change in air density and the refractive index, both quantities decrease in the same direction as the wind. Because light bends in the direction of an increasing refractive index, the laser beam shifts its peak intensity in the upwind direction.

This effect can be roughly quantified by assuming steady-state thermal blooming, in which $\partial \Delta T / \partial t = 0$ in Equation (9), and that the wind velocity is entirely along the transverse x-direction, so $\mathbf{v} = v\hat{i}$. The phase shift (in rad) from thermal blooming can then be written as [11]

$$\varphi_B(x, y, z) = ik \int_0^z \delta n \, dz = -\frac{n_0 - 1}{T_o} \frac{\alpha k z}{\rho C_p v} \int_{-\infty}^x I \, dx' ,\tag{11}$$

where the beam is assumed to be collimated along the z-direction. If we further assume an irradiance distribution for a Gaussian beam, Equation (11) can be solved analytically to obtain [11]

$$\varphi_{BG}(x, y, z) = -\frac{\Delta \varphi_G}{2} \exp\left[-(y/a)^2\right]\left[1 + erf(x/a)\right],\tag{12}$$

$$\cong -\frac{\Delta \varphi_G}{2}\left\{1 + \frac{2}{\sqrt{\pi}}\left(\frac{x}{a}\right) - \left(\frac{y}{a}\right)^2 - \frac{2}{\sqrt{\pi}}\left[\frac{1}{3}\left(\frac{x}{a}\right)^3 + \left(\frac{x}{a}\right)\left(\frac{y}{a}\right)^2\right] + \frac{1}{2}\left(\frac{y}{a}\right)^4 \ldots\right\},\tag{13}$$

where the maximum phase shift across the beam $\Delta \varphi_G$ can be expressed as

$$\Delta \varphi_G = \left(\frac{1}{2\sqrt{\pi}}\right) N_D\tag{14}$$

and

$$N_D = \frac{2(n_0 - 1)k\alpha P z}{\rho C_p v a T_o} .\tag{15}$$

The N_D parameter represents the Bradley-Hermann [13] distortion number and is utilized as a quantitative measure for the intensity of thermal blooming [11]. Blooming becomes a significant complication to the propagation of laser energy when $N_D > 25$ [4].

The effects of phase distortion on the laser beam can be specifically inferred from the series expansion in Equation (13). The leading (x/a) term produces the deflection of the laser beam along the wind direction in the x-direction and the leading $(y/a)^2$ term produces the beam divergence in the y-direction [11].

4.   Laser Beam Irradiance Pattern Due to Thermal Blooming

The thermal blooming irradiance pattern can be estimated for the phase accumulation φ_{BG} by solving the paraxial wave equation in the ray-optics limit using perturbation theory. To the first-order perturbation, the solution follows as [11]

$$\frac{I(x,y,z)}{I_0 e^{-\epsilon z}} = exp\left\{-N_c\left[2\frac{x}{a}e^{-(x^2+y^2)/a^2} + \frac{\sqrt{\pi}}{2}e^{-\frac{y^2}{a^2}}\left(1-\frac{4y^2}{a^2}\right)\left[1+\text{erf}(x/a)\right]\right]\right\}, \quad (16)$$

where I_0 is the unperturbed, Gaussian, collimated beam profile and N_c is the collimated beam irradiance distortion parameter with the inclusion of wind effects, taking the form of [11]

$$N_c = \frac{(n_0-1)\alpha P z^2}{\pi n_0 \rho C_p T v a^3}. \quad (17)$$

In general, an increase in the beam distortion parameter represents a greater effect of thermal blooming on the laser beam and results in an irradiance pattern taking the form of a crescent shape, which is illustrated in Figure 6.
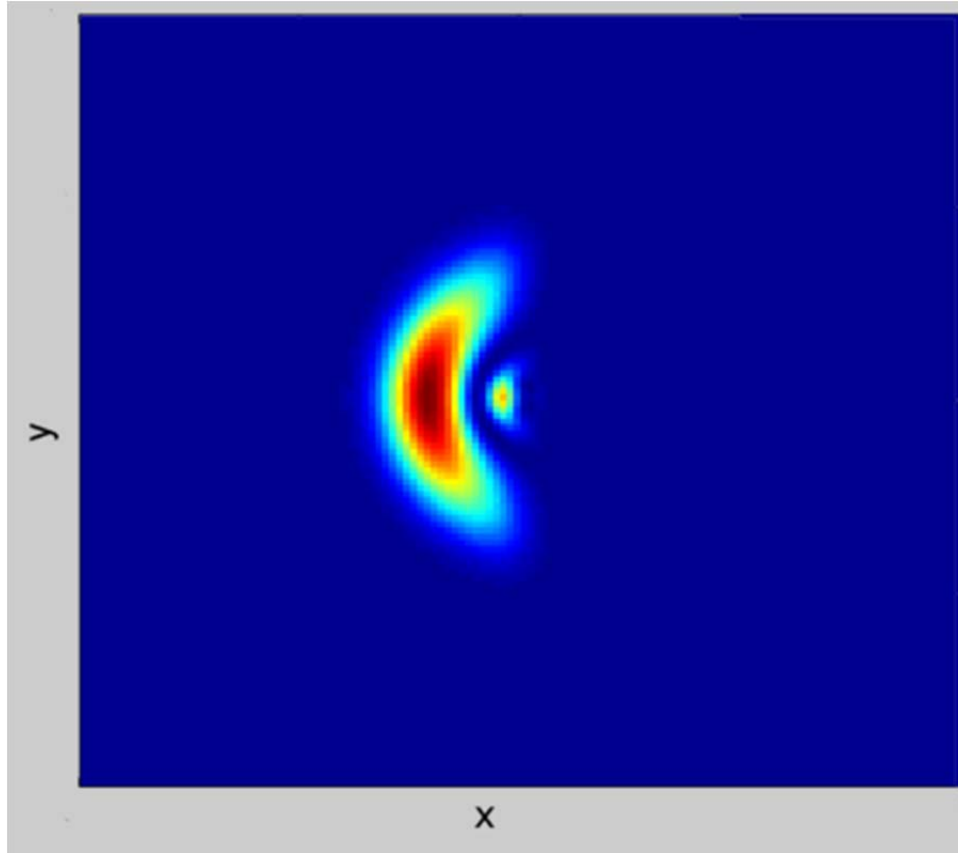
Figure 6.   The general transverse laser beam profile due to the effects of steady-state thermal blooming. The presence of wind moving from left to right in the figure results in the typical crescent shape shown. The color map indicates the irradiance of the laser beam, with the dark red color representing the highest irradiance and the dark blue the lowest. The scale of beam deflection depends upon the distance to the target, beam power, atmospheric extinction, and other parameters as described in the text.

THIS PAGE INTENTIONALLY LEFT BLANK

IV.   ATMOSPHERIC CODE OVERVIEW

Effective employment of HEL weapon systems requires knowledge of the atmospheric optical properties and how these properties affect laser propagation. The atmospheric parameters that determine these optical properties are extremely complicated and depend on pressure, temperature, humidity, aerosol size composition, etc. Furthermore, all of these parameters are functions of elevation, time of day, and season.

Due to these complications, it is difficult to fully map out this multi-dimensional parameter space for varying altitudes with experimental data. Thus, a means of generating optical properties based upon known physical principles for a large range of conditions must be employed, which can then be used to evaluate laser beam propagation.

A.   MOLECULAR ABSORPTION: α_a

Among the primary atmospheric optical properties that govern laser beam propagation are the four components of the extinction coefficient (See Chapter II, Section A). A combination of measurements and quantum theory is utilized to determine the first component, the molecular absorption coefficient α_a, which represents the absorption of laser energy by molecules in the atmosphere.

Within the electromagnetic spectrum, the position and strength of absorption features at each wavelength arise from quantized molecular energy levels. The atmospheric codes which are employed in atmospheric modeling query a database of absorption features (such as the HITRAN database), modify the line shapes based upon temperature and pressure, and then add them together to get the absorption coefficient at a specific wavelength. This method is based on assumptions regarding the natural line shape and how temperature and pressure affect the shape.

1. Assumptions

The general form of an absorption coefficient line shape α_a is represented by

$$\alpha_a = NSf\left(v - v_o\right), \tag{18}$$

where N represents the number of atoms per unit volume, S is the line strength, $f\left(v - v_o\right)$ is the normalized line shape at frequency v, and v_o is the central frequency of the line, where $\int_0^\infty f\left(v - v_o\right)\,dv = 1$. One of the most fundamental assumptions regarding molecular absorption modeling is that the natural line shape for each absorption feature is based upon modeling a molecular electron as a damped, driven harmonic oscillator, with the equation of motion given by [9]:

$$\frac{\bar{F}}{m_e} = \frac{e\bar{E}}{m_e} = \ddot{\bar{r}} + 4\pi\Gamma_n\dot{\bar{r}} + \xi\bar{r}\,. \tag{19}$$

In Equation (19), $\bar{F}$ represents the force vector, m_e is the mass of the electron, e is the charge of the electron, $\bar{E}$ is the total electric field (including the contribution from the light), $\ddot{\bar{r}}$ is the electron acceleration, Γ_n is the effective natural damping constant, $\dot{\bar{r}}$ is the electron velocity, ξ is related to the strength of the restoring force (which is related to the effective spring constant), and $\bar{r}$ is the electron position. While the potential energy of molecular bonds, also known as the Morse potential, is not the same as a harmonic oscillator, at lower energy levels it can be reasonably approximated by the harmonic potential, as shown in Figure 7, thus providing motivation for using Equation (19). This approximation is nominally satisfied at typical atmospheric conditions, as most of molecular electrons remain in their ground energy state at standard temperature and pressure (STP).
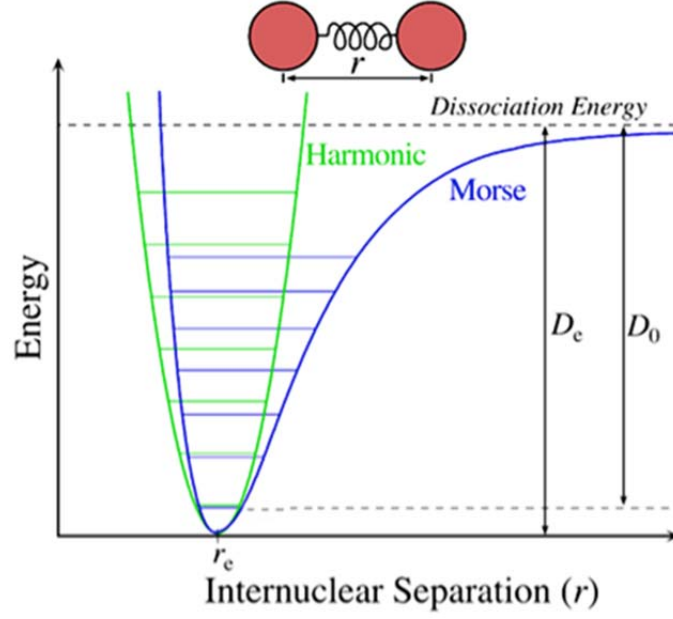
Figure 7.   Harmonic oscillator approximation. At low energy levels and small internuclear separation, the Morse potential can be adequately approximated by the harmonic potential, after [15].

Equation (19) can be used to determine the complex refractive index [9]. The imaginary part of the refractive index is responsible for absorption and determines the functional shape of $f(v - v_o)$ as

$$f(v - v_o) = \frac{1}{\pi} \frac{\Gamma_n}{(v - v_o)^2 + \Gamma_n^2},$$ (20)

where Γ_n is the same effective damping constant in Equation (19). Equation (20) is in the form of a Lorentzian, with Γ_n also specifying the full-width half-maximum of the response, as visualized in Figure 8.
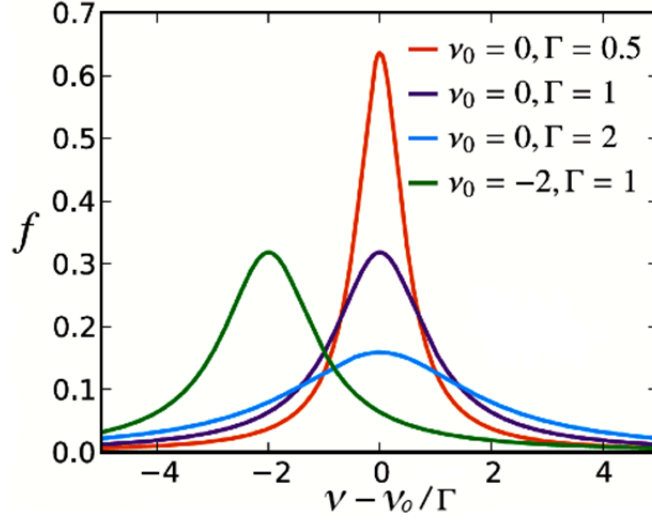
Figure 8.   The dependence of spectral line width $f(v - v_o)$ and height on resonant frequency and damping, respectively, after [16].

2.   Absorption Line Broadening

The absorption spectrum of a single line is broken down into the shape and strength of the line as described by Equation (18). However, various mechanisms affect these spectral line characteristics, which are discussed below.

a.   Natural Line Width

The natural line width of an absorption feature is characterized by the damping of the harmonic oscillator vibrations due to energy emission of the molecule [9]. The Heisenberg uncertainty principle can be used to estimate the width of the absorption line and thus provides a means of estimating Γ_n. It states

$$\Delta E \, \Delta t \geq \frac{h}{2\pi}, \tag{21}$$

$$\Delta v = \frac{\Delta E}{h} = \frac{1}{2\pi\Delta t}, \tag{22}$$

where ΔE is the change in energy of the molecule for a particular transition, Δt is the lifetime of the excited state, h is the Planck constant, and Δv is the width of the line shape.

26

In the thermal infrared regime, the lifetimes of isolated molecules are $\Delta t \approx 0.1 - 10$ s, in which case the width of the lineshape $\Delta v \sim 0.3$ Hz, which means the damping constant Γ_n is similarly small. Because the natural line width determined from the uncertainty principle and modeled by quantum mechanics is very small, the effects of the two broadening mechanisms discussed below dominate the spectral line shapes and Γ_n can be neglected.

b. Pressure Broadening

As stated earlier, two broadening mechanisms dominate the characteristic shape of spectral lines. Pressure broadening is a mechanism by which molecular collisions in the atmosphere transfer energy between molecules, thereby reducing the lifetime of higher energy states and increasing the effective damping of the oscillator. It is the dominant broadening mechanism in the lower atmosphere below ~ 20 km [14]. Increased pressure causes more collisions that broaden the Lorentzian absorption lines, taking the form of

$$f_P(v - v_0) = \frac{\Gamma_P / \pi}{(v - v_0)^2 + \Gamma_P^2},$$ (23)

where Γ_P is the effective damping constant due to collisions and is many orders of magnitude larger than Γ_n [14]. The damping constant Γ_P is determined from the mean time between inelastic molecular collisions t_c, so that $\Gamma_P = 1/2\pi t_c$. It also follows the trend

$$\Gamma_P = \Gamma_0 \left(\frac{p}{p_0} \right) \left(\frac{T_0}{T} \right)^n,$$ (24)

where Γ_0 represents the line width at a reference temperature T_0 and pressure p_0, and $n \approx 1/2$ is determined empirically [9].

Figure 9, below illustrates the Lorentz line shape for three pressure values. For typical vibration-rotation bands, a line width of 1.5×10^9 Hz at a pressure of one bar is typical [17].

27
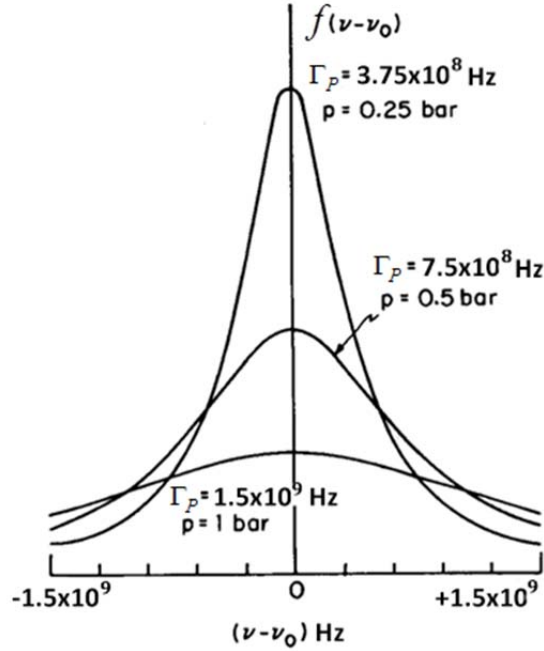
Figure 9.   Lorentz line shape caused by pressure broadening, with variations in damping constant and atmospheric pressure, after [14].

c.   Doppler Broadening

Doppler shifts also serve to broaden spectral line shapes. As laser energy propagates through the atmosphere, the light encounters molecules with a random distribution of velocities. A Doppler frequency shift due to molecular motion results in a further broadening of the emission/absorption spectrum, but in a Gaussian profile described by [18]

$$f_D\left(v-v_0\right)=\frac{1}{\Gamma_D\sqrt{\pi}}\exp\left[-\frac{\left(v-v_0\right)^2}{\Gamma_D{}^2}\right],\tag{25}$$

$$\Gamma_D=v_0\sqrt{\frac{2k_BT}{mc^2}},\tag{26}$$

where Γ_D is the Doppler line half-width, k_B is the Boltzmann constant, m is the mass of the molecule and c is the speed of light.

Since a change in temperature implies a change in the velocity of molecular motion, an increase in temperature generally correlates to an increase in Doppler broadening.

d. Voigt Profile

Atmospheric codes use Voigt profiles to combine the effects of pressure (Lorentzian) and Doppler (Gaussian) broadening mechanisms. The Voigt line shape is quantitatively described by [14]

$$f_V (v - v_0) = \frac{\Gamma}{\pi^{3/2} \Gamma_D} \int_{-\infty}^{+\infty} \frac{e^{-y^2}}{(x - y)^2 + \Gamma^2} dy ,$$

(27)

where $\Gamma = \Gamma_P / \Gamma_D$ and $x = (v - v_0) / \Gamma_D$. The Voigt profile is illustrated in Figure 10.
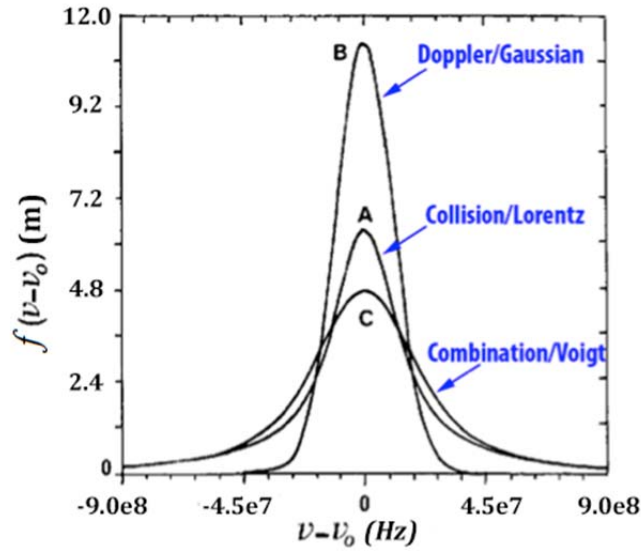
Figure 10.   Collision, Doppler and Voigt spectral line profiles, after [14].

In the shoulders of the line shape, the Voigt profile exhibits a Lorentzian shape, while a resemblance to the Gaussian shape is seen near the center of the line shape.

3.   Continuum Absorption

Although the Voigt profile is a well-known representation of spectral line shapes, it is not completely devoid of error. Continuum absorption, a phenomenon discovered in 1918, represents the discrepancy between such data obtained from a mathematical summation of Voigt lines and actual measurement data of the molecular absorption spectrum.

29

The physical principles behind continuum absorption remain debated; however, a couple of theories attempt to reconcile the difference between experimental and modeling data. One possible explanation lies in the hypothesis that actual absorption line shapes are not perfectly modeled by the Voigt profile, and a summation over thousands of such lines gradually yields a rather significant margin of error. Another possible explanation lies in the tendency of water to form dimers in the atmosphere. A dimer consists of two H_2O molecules loosely-bound with a hydrogen bond, exhibiting measured dissociation energy of $\sim 13.2 \pm 0.12 \, kJ / mol$ [19]. Incident laser light upon such dimers could cause the beam to deposit extra energy into the atmosphere, resulting in an absorption spectrum which is not properly modeled by the Voigt profile.

Whatever the mechanism, continuum absorption varies slowly with wavelength, and thus atmospheric codes often add the contribution from continuum absorption using the semi-empirical Clough-Kneizys-Davies (CKD) continuum model [20].

B.   MIE SCATTERING THEORY: α_a, β_m, AND β_a

While a combination of measurements and quantum theory is utilized to determine the first component of the extinction coefficient, a separate solution called Mie scattering is used to determine the latter three components.

1.   Theory Introduction

Mie scattering theory describes the interaction between electromagnetic radiation and small particles suspended in the atmosphere, such as dust and aerosols [9]. The theory is utilized to determine the molecular scattering coefficient β_m, as well as the aerosol absorption coefficient α_a and aerosol scattering coefficient β_a. Mie theory contains three key assumptions, the first of which states that all atmospheric particles are spherical in shape. The second assumption states that the scattering particles are homogeneous in material and thus can be represented by a single complex refractive index $\tilde{n}$. The last assumption holds that the light incident upon a particle, in this case from the laser, is in the form of a plane wave.

While these assumptions simplify the interaction of light and atmospheric particles, they do not always represent reality. For example, many particles such as cubic salt crystals are not spherically shaped. However, Mie scattering theory can still be applied in that case since the irregular particles are suspended in a turbulent media and are not preferentially oriented in one direction [21]. More sophisticated codes extend Mie scattering to include spheres with layers of thin films for various purposes, such as modeling water layers on aerosol particles [22].

2. Amplitude Scattering Matrix

In calculating the atmospheric extinction coefficients, the initial goal of Mie scattering theory is to determine the scattered field amplitude at an angle θ and a specified distance r from a scattering object, in this case a suspended particle or aerosol [9]. While Mie theory utilizes Maxwell's equations to determine the solutions to the fields, both inside and outside of the scattering object or scatterer, HEL propagation only concerns "far-field" scattering, where $r \gg a^2/\lambda$ and a is the particle radius. In this case, the fields take the form of [9]

$$\begin{bmatrix} E_s^{\parallel}(r,\theta) \\ E_s^{\perp}(r,\theta) \end{bmatrix} \approx \frac{\exp(-ikr)}{ikr} \begin{bmatrix} S_2(\theta) & 0 \\ 0 & S_1(\theta) \end{bmatrix} \begin{bmatrix} E_i^{\parallel} \\ E_i^{\perp} \end{bmatrix}, \tag{28}$$

where $E_i^{\parallel}$ and $E_i^{\perp}$ are the parallel and perpendicular components of the incident electric field and $E_s^{\parallel}$ and $E_s^{\perp}$ are the respective components of the scattered electric field. The wavenumber $k = 2\pi/\lambda$ is representative of light in air since the refractive index of air $\tilde{n} = 1$. The amplitude scattering matrix $\begin{bmatrix} S_2(\theta) & 0 \\ 0 & S_1(\theta) \end{bmatrix}$ determines the amount and polarization of scattered light at a given angle θ measured with respect to the incident light.

The scattering amplitudes S_1 and S_2 take the form of [23]

$$S_1(\theta) = \sum_{\ell=1}^{\infty} \frac{2\ell+1}{\ell(\ell+1)} \left[a_\ell \pi_\ell(\cos\theta) + b_\ell \tau_\ell(\cos\theta) \right], \tag{29}$$

31

$$S_2(\theta) = \sum_{\ell=1}^{\infty} \frac{2\ell+1}{\ell(\ell+1)} \left[b_\ell \pi_\ell(\cos\theta) + a_\ell \tau_\ell(\cos\theta) \right], \tag{30}$$

where π_ℓ and τ_ℓ depend only on the scattering angle θ and are defined as [23]

$$\pi_\ell(\cos\theta) = \frac{1}{\sin\theta} P_\ell^1(\cos\theta), \tag{31}$$

$$\tau_\ell(\cos\theta) = \frac{d}{d\theta} P_\ell^1(\cos\theta). \tag{32}$$

In Equations (31) and (32), P_ℓ^1 is the associated Legendre polynomial. The Mie coefficients a_ℓ and b_ℓ are dependent only on the optical wavelength λ, the scatterer radius a, and the scatterer index of refraction $\tilde{n}$, and are defined as [23]

$$a_\ell = \frac{\xi_\ell(k_1 a)\xi_\ell'(k_2 a) - (\eta_1/\eta_2)\xi_\ell(k_2 a)\xi_\ell'(k_1 a)}{\zeta_\ell(k_1 a)\xi_\ell'(k_2 a) - (\eta_2/\eta_1)\xi_\ell(k_2 a)\zeta_\ell'(k_1 a)}, \tag{33}$$

$$b_\ell = \frac{(\eta_2/\eta_1)\xi_\ell(k_1 a)\xi_\ell'(k_2 a) - \xi_\ell(k_2 a)\xi_\ell'(k_1 a)}{(\eta_2/\eta_1)\zeta_\ell(k_1 a)\xi_\ell'(k_2 a) - \xi_\ell(k_2 a)\zeta_\ell'(k_1 a)}, \tag{34}$$

where ξ_ℓ, ξ_ℓ', ζ_ℓ, and ζ_ℓ' denote the Hankel functions [19].

3. Total Cross Sections

The total scattering cross section integrated over all angles takes the form of [9]

$$\sigma_s = \frac{\lambda^2}{2\pi} \sum_{\ell=1}^{\infty} (2\ell+1)\left(|a_\ell|^2 + |b_\ell|^2\right). \tag{35}$$

The extinction (scattering + absorption) cross section is given by

$$\sigma_e = \frac{\lambda^2}{2\pi} \sum_{\ell=1}^{\infty} (2\ell+1)\Re\left(a_\ell + b_\ell\right), \tag{36}$$

where $\Re(\ldots)$ denotes the real part. Finally, the total absorption cross section is [9]

$$\sigma_a = \sigma_e - \sigma_s, \tag{37}$$

which is simply the difference between the extinction and scattering cross sections. The absorption and extinction coefficients are calculated from their respective cross-sections

by integrating over the contributions from different particle sizes. For example, the aerosol scattering coefficient β_a is calculated by integrating [9]

$$\beta_a(\lambda) = \int_{r_1}^{r_2} N(r)\sigma_s(r)dr, \tag{38}$$

where $N(r)dr$ is the number of particles with a radius between r and $r + dr$ per unit volume.

4.   Rayleigh Scattering Limit for Determining β_m

Molecular scattering assumes that particles of size a are much smaller than the wavelength of the laser light $(a \ll \lambda)$. In the Rayleigh scattering limit, the scattering cross-section depends on the wavelength of electromagnetic energy as $\propto \lambda^{-4}$, so shorter wavelengths scatter more readily. A famous example of this principle is the color of the daytime sky: because blue light is of a shorter wavelength than red light, it Rayleigh scatters more readily and thus the sky appears blue.

In this case, the Rayleigh scattering approximation can be utilized to determine the scattering cross section by [9]

$$\sigma_s \approx \frac{128\pi^5}{3} \frac{a^6}{\lambda^4} \left(\frac{n^2 - 1}{n^2 + 2} \right)^2, \tag{39}$$

$$n^2 = |\tilde{n}|^2. \tag{40}$$

The molecular scattering coefficient can then be calculated from the cross section following the same method as Equation (38).

Figure 11 visualizes the general scattering cross section-dependent trends associated with Mie scattering theory. In the low-frequency regime the circumference of an arbitrary spherical particle is smaller than the wavelength of energy passing over it, and thus Rayleigh scattering ($\propto \lambda^{-4}$) describes the scattering cross section σ_s.
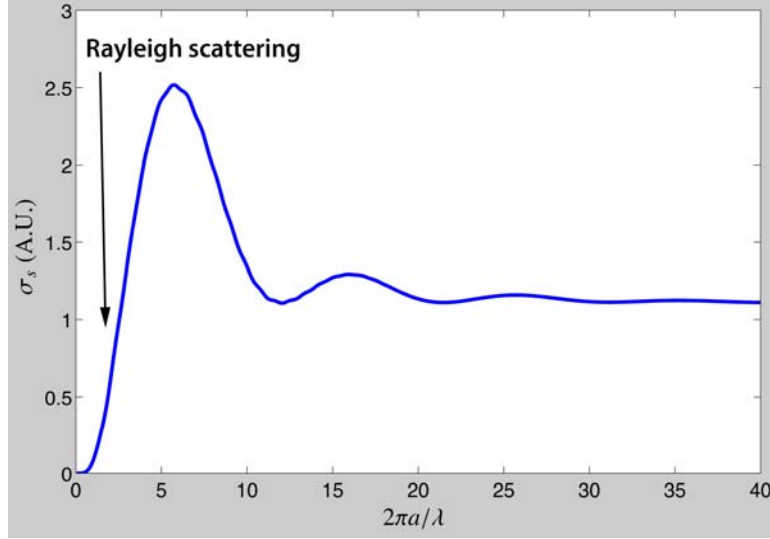
Figure 11.   Mie theory scattering behavior with respect to the cross-section of
the scatterer. The Rayleigh scattering limit is indicated in the figure.

5.   Aerosol Absorption and Scattering Coefficients α_a and β_a

Aerosol sizes are typically on the order of an optical wavelength $(a \approx \lambda)$. According to Mie theory, aerosol-sized particles scatter and absorb electromagnetic energy in a manner weakly dependent on the wavelength of light passing through them [9]. Figure 11 visualizes this trend: In the high frequency (optical) limit characterized by the resonance when $a \approx \lambda$, the cross section is roughly independent of the wavelength. As previously stated, the aerosol absorption and scattering coefficients are calculated following the method in Equation (38). However, unlike the Rayleigh scattering approximation for calculating β_m, aerosol coefficients have no similar approximating solutions.

C.   MODTRAN

There are several well-established radiative transfer codes that are used to generate extinction coefficients needed to model laser propagation. One of the most widely used of these is MODTRAN (MODerate resolution atmospheric TRANsmission) [25], a band-transmission code, which utilizes a database of pre-calculated coefficients

34

for a wide variety of atmospheric conditions and aerosol content. MODTRAN uses the HITRAN database for molecular absorption spectra [26].

MODTRAN is a relatively fast (but potentially less accurate) method of obtaining optical properties compared to other much more computationally intensive codes such as the line-by-line LBLRTM program [27]. The reason line-by-line codes are more CPU intensive is that they first sum over all absorption lines, then add continuum absorption for a specific wavelength, then calculate Mie absorption and scattering coefficients from physical principles to finally determine the extinction coefficient.

However, while MODTRAN may be a potentially less accurate means of generating optical properties, the program is very flexible as it allows for various atmospheric parameters to be set by the user.

1. Preset Atmospheric Models

Table 2 lists the six atmospheric model presets that MODTRAN can use to generate atmospheric optical properties. The user can utilize one of these presets as is, modify aspects of these presets, or specify user-defined models.

Atmospheric Model #	Description
1	Tropical Atmosphere (15° Latitude)
2	Mid-Latitude Summer (45° North Latitude)
3	Mid-Latitude Winter (45° North Latitude)
4	Sub-Arctic Summer (60° North Latitude)
5	Sub-Arctic Winter (60° North Latitude)
6	1976 US Standard Atmosphere

Table 2.   MODTRAN preset atmospheric models, after [25].

The six preset models vary in several characteristics, most importantly in their temperature, H_2O, and O_3 profiles. Figure 12 displays the temperature profiles as functions of altitude for each of these presets [25].
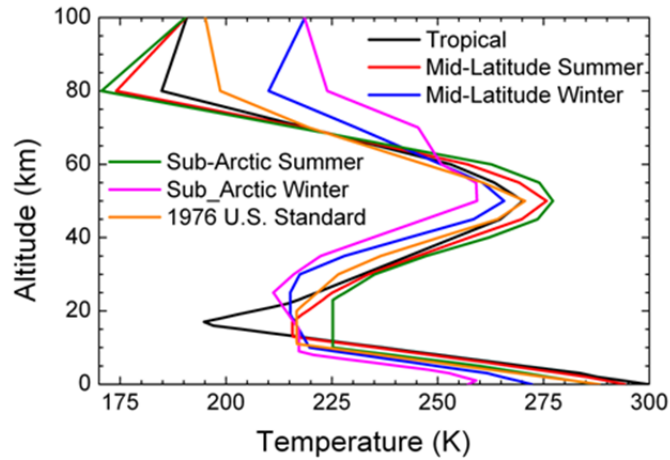
Figure 12.   MODTRAN model atmosphere temperature profiles. The varying colors indicate temperature profiles for the different model atmospheres, from [25].

Naturally, the Sub-Arctic Winter preset exhibits the coldest surface temperature while the Tropical model exhibits the warmest.

Figure 13 displays the H_2O and O_3 profiles as functions of altitude for the six preset atmospheres [25].
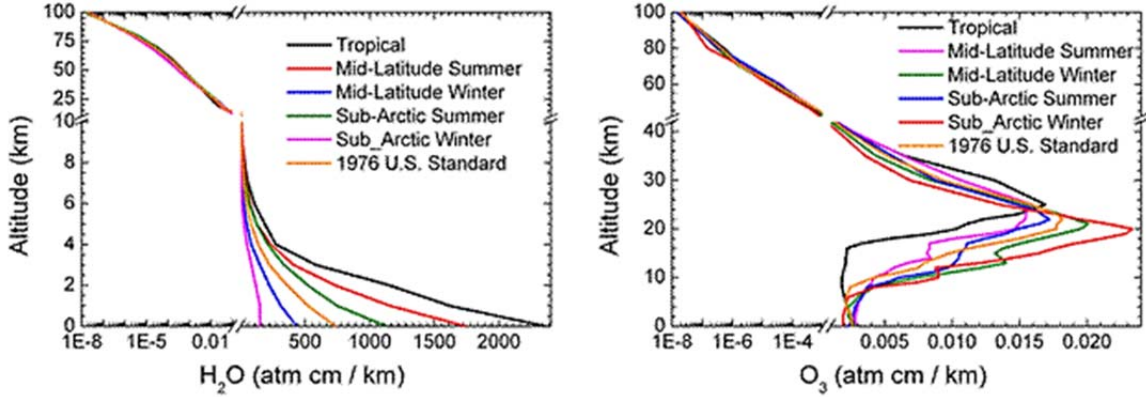
Figure 13.   MODTRAN model atmosphere H_2O and O_3 profiles. The gaps in the data are the result of the breaks in the vertical and horizontal axes, as indicated, from [25].

As expected, the Tropical model atmosphere contains the highest concentration of H_2O at the surface and the Sub-Arctic Winter contains the lowest. The O_3 profile is slightly more complicated, with all models containing a roughly equal concentration at ground level, and varying greatly at the peak at ~ 20 km, which represents the ozone layer.

2.   Meteorological Range Presets

MODTRAN allows for varying aerosol densities by specifying the ground meteorological range presets at 23, 15, 10 or 5 km. Meteorological range (MR), in this case, is defined by Equation (49) as [25]

$$MR[km] = \frac{\ln(50)}{EXT550[km^{-1}] + 0.01159 km^{-1}},$$ (41)

where $EXT550[km^{-1}]$ represents the surface aerosol extinction at 550 nm and $0.01159 km^{-1}$ is the surface Rayleigh scattering coefficient at 550 nm. Meteorological range can also be equated to the more subjective visibility, defined as the maximum distance at which an individual can spot and identify a prominent object along the horizon at day (or a light at night), by the approximate Equation (42)

$$Visibility \approx \frac{MR}{1.3 \pm 0.3}.$$ (42)

If no meteorological range is specified, a default value is generated from presets associated with the boundary layer chosen in the particular aerosol model (see next section).

3. Aerosol Models

Another option within MODTRAN specifies the aerosol model preset used for the surface layer (from zero to two kilometers above sea level) that also includes a default surface-meteorological range. While MODTRAN also allows the user to specify aerosol models at altitudes above the surface layer, this thesis will only consider engagements below two kilometers. The surface layer atmospheric extinction coefficient dependence on the relative humidity is determined by the water-vapor content of the selected atmosphere model. Table 3 lists the primary aerosol presets available in MODTRAN, with model #7 as the user-specified aerosol extinction coefficient option excluded.

Aerosol Model #	Description
0	No aerosol or cloud attenuation
1	RURAL model; Default meteorological range set to 23 km
2	RURAL model; Default meteorological range set to 5 km
3	NAVY MARITIME model; Default meteorological range set based on wind speed & relative humidity
4	MARITIME model; Default meteorological range set to 23 km
5	URBAN model; Default meteorological range set to 5 km
6	TROPOSPHERIC model; Default meteorological range set to 50 km
8	FOG1 model (Advective Fog); Default meteorological range set to 0.2 km
9	FOG2 model (Radiative Fog); Default meteorological range set to 0.5 km
10	DESERT model; Default meteorological range set by wind speed

Table 3.   MODTRAN main aerosol and cloud options, after [25].

The preset most commonly used in this study was the #4 Maritime model, with a default ground meteorological range of 23 km. The primary purpose of the Maritime model is to study the propagation of infrared energy through the atmosphere in the near sea surface layer, an area in which all Naval vessels would operate in, making the model useful for this research.

This model utilizes an aerosol profile composed of a sea-salt component and a continental component, the latter of which is primarily comprised of water soluble material such as ammonium, calcium sulphate, and other organic compounds. This aerosol profile does not contain any larger dust particles due to the assumption that these particles would rapidly fall out of the atmosphere as a result of gravitational settling, which occurs on the order of hours to days as the air moves from land and across the ocean [21].

Furthermore, the Maritime model also neglects the effects of fresh sea-spray, which occurs in the lower altitudes above the sea surface at 10-20 meters and is strongly dependent on surface wind speed. Other Maritime aerosol models are available in MODTRAN that include these sea-spray effects and could represent a possible extension to this research.

4.   Cloud and Rain Models

Additional options specify the cloud and rain presets utilized by MODTRAN in generating atmospheric extinction coefficients. The rain profiles decrease linearly from the ground to the top of the associated cloud model, with the rain cutting off at the cloud top [20]. Table 4 lists the major MODTRAN cloud and rain models, with preset # 11 as the user-specified cloud extinction and absorption coefficient option excluded.

Rain Model #	Description
0	No clouds or rain
1	Cumulus cloud layer with base at 0.66 km and top at 3.0 km
2	Altostratus cloud layer with base at 2.4 km and top at 3.0 km
3	Stratus cloud layer with base at 0.33 km and top at 1.0 km
4	Stratus/stratocumulus cloud layer with base at 0.66 km and top at 2.0 km
5	Nimbostratus cloud layer with base at 0.16 km and top at 0.66 km
6	2.0 mm/hr ground Drizzle (Includes ICLD # 3 with 0.86 mm/hr rain at 1.0 km)
7	5.0 mm/hr Light rain (Includes ICLD # 5 with 2.6 mm/hr rain at 0.66 km)
8	12.5 mm/hr ground Moderate rain (Includes ICLD # 5 with 6.0 mm/hr rain at 0.66 km)
9	25.0 mm/hr ground Heavy rain (Includes ICLD # 1 with 0.2 mm/hr rain at 3.0 km)
10	75.0 mm/hr ground Extreme rain (Includes ICLD # 1 with 1.0 mm/hr rain at 3.0 km)
18	Standard Cirrus model with 64 μm mode radius for ice particles
19	Sub-visual Cirrus model with 4 μm mode radius for ice particles

Table 4.   MODTRAN cloud and rain models, after [25].

D.   LEEDR

LEEDR (Laser Environmental Effects Definition and Reference) is a MATLAB-based atmospheric modeling program created by the Air Force Institute of Technology (AFIT), and serves a similar function as MODTRAN in characterizing a location's atmosphere based on various user inputs such as location, weather, etc. [28]. Because using MODTRAN to generate optical parameters for model atmospheres containing variable amounts of precipitation proved unsuccessful, LEEDR was thus implemented to obtain this data set. All LEEDR-generated rainy model atmospheres were calculated using atmosphere types and aerosol models corresponding to those available in MODTRAN. While there were slight variations in the final propagation results obtained from the model atmospheres generated by MODTRAN and LEEDR, the data strongly agreed at the 1.064 μm wavelength (which corresponds to the nominal laser wavelength for the SSL).

V. SIMULATION METHODS

In order to accurately and efficiently model HEL propagation in various atmospheric conditions, NPS has developed ANCHOR (Atmospheric NPS Code for HEL Optical pRopagation). ANCHOR is a succinct Matlab script that utilizes pre-calculated data sets containing extinction coefficient values across a specified wavelength spectrum. The components of the extinction coefficient – namely the molecular and aerosol absorption and scattering coefficients (see Chapter III, Section A) – and specified laser parameters are subsequently integrated into the scaling equations governing laser propagation. The on-target laser irradiance and power-in-the-bucket values are obtained across a specified wavelength spectrum.

Four specific effects govern the behavior of the beam as it propagates to the target: Diffraction, turbulence, platform jitter, and thermal blooming. The linear effects of diffraction, turbulence and jitter are assumed to produce a time-averaged Gaussian irradiance profile, and can be evaluated independently of each other. These effects are all implemented within the "master Equation (43) [29]," which describes the time-averaged irradiance, or intensity, $\langle I \rangle$ of the laser beam on a target (in W/m^2).

$$\langle I \rangle \approx \frac{P_{tot}}{\pi \langle w_{tot} \rangle^2} e^{-\epsilon \ell} S_{TB} . \tag{43}$$

In Equation (43), P_{tot} represents the total output power from the laser beam director, $\langle w_{tot} \rangle$ is the time-averaged radius ($1/e$ in the intensity) of the laser spot on target. The $e^{-\epsilon \ell}$ factor comes from Beer's law (see Chapter III, Section A), where ϵ is the total extinction coefficient due to atmospheric absorption and scattering (in m^{-1}) and ℓ is the distance (in m) from the beam director to the target. The S_{TB} factor represents the thermal blooming Strehl ratio, which accounts for the non-linear reduction in the on-axis irradiance due to thermal blooming.

The total laser beam spot size on target $\langle w_{tot} \rangle$ is determined by [29]

$$w_{tot}{}^2 = w_d{}^2 + w_t{}^2 + w_j{}^2 , \tag{44}$$

in which w_d represents the root-mean-square (rms) spot size due to only diffraction in a vacuum, w_t the rms spot size due to only turbulence, and w_j the rms spot size due to only platform jitter. Since these effects are independently assumed to result in time averaged Gaussian irradiance patterns, their combined rms contributions add in quadrature.

A.   LINEAR EFFECTS

Before the linear effects of diffraction, turbulence and jitter governing the behavior of a propagating laser beam can be implemented into Equation (43), they have to be first considered and quantified independently.

1.   Vacuum Diffraction: w_d

The effects of laser beam diffraction in a vacuum can be quantified by estimating the beam's spot size due to diffraction, which follows as

$$w_d \approx M \frac{2\lambda\ell}{\pi D}, \tag{45}$$

where D represents the beam diameter at the source and M represents the mode factor measuring beam quality. If the laser has a uniform transverse beam shape, then D is also the diameter of the beam director; for a Gaussian shape, it represents the diameter of the beam at the $1/e$ point in the irradiance. The mode factor is a unit-less parameter which represents the mode content of a multimode laser beam obtained from a stable resonator. The square of M, the M^2 parameter, compares the product of beam divergence Θ (in rad) and spot size w of a real laser beam to that of a fundamental Gaussian reference beam, so that [30]

$$M^2 = \frac{\Theta w}{\Theta_{ref} w_{ref}}, \tag{46}$$

where Θ_{ref} represents the reference beam divergence and w_{ref} the reference beam spot size. The M^2 parameter is a widely used quality metric for laser beams, and as such is often defined as the "beam quality" factor. However, a more accurate definition of M^2 is

the "beam propagation" factor, since the parameter ultimately provides a measure of how the beam will propagate through free space [31]. For an ideal Gaussian beam, $M^2 = 1$, while for a non-ideal beam, $M^2 > 1$. An M^2 value less than unity is not possible.

The spot size due to diffraction can be further described by taking into account the laser beam's focal range F, which yields

$$w_d^2 = \frac{M^2 \ell^2}{k^2 w_s^2} + w_s^2 \left(1 - \frac{\ell}{F}\right)^2, \tag{47}$$

where the wavenumber $k = 2\pi / \lambda$ and w_s represents the laser beam radius at the source. For this research, the focal point of the laser beam was placed on the target, so $F = \ell$ and the second term in (47) is eliminated.

2. Atmospheric Turbulence: w_t

Turbulence is described comprehensively in Chapter III, Section B. The effect of turbulence on the laser spot size on target can be estimated by

$$w_t \approx \frac{2\pi \ell}{\pi r_0}, \tag{48}$$

where ℓ once again represents the distance to target and r_0 is the Fried parameter, which defines a length scale within which the laser beam maintains transverse coherence during its propagation path. The Fried parameter is estimated by

$$r_0 \approx 3.03 \left[\left(\frac{2\pi}{\lambda}\right)^2 C_n^2 \ell \right]^{-0.6}, \tag{49}$$

where C_n^2 characterizes the strength of the turbulence, as discussed in Chapter III, Section B.

3. Platform Jitter: w_j

Platform jitter is defined as the randomized movement of the laser spot position on the target due to the motion of the laser platform as well as tracking error by the active or passive tracking system. The time-averaged effect of jitter can be quantified by

considering Equation (50), where θ_{rms} defines the total rms angular displacement (in rad) due to all contributions from jitter and ℓ is the distance (in m) to target:

$$w_j \approx \theta_{rms}\ell. \tag{50}$$

B. THERMAL BLOOMING

As previously discussed, thermal blooming describes the non-linear phenomenon in which ambient air surrounding the propagating laser beam is heated by the beam itself, resulting in a change in the local air density. This change in air density results in a change in the refractive index of the local atmosphere, creating a "lens" in the air that causes the beam to diverge. The direct effect of thermal blooming is the reduction of the laser beam irradiance on target. Thermal blooming is discussed extensively in Chapter III, Section C.

1. Distortion Number: N_D

The effects of thermal blooming can be characterized by the thermal distortion number N_D (Chapter III, Section C.3), which is defined as [4]:

$$N_D = \frac{-4\sqrt{2}kP_{tot}}{\rho_0 C_p} \int_0^\ell \frac{\alpha(z)T(z)n_T(z)}{v(z)D(z)} dz, \tag{51}$$

where the wavenumber $k = 2\pi/\lambda$, $\rho_0 \sim 1 \text{ kg}/\text{m}^2$ represents the ambient air density, $C_p \sim 10^3$ J/kg-K is the specific heat of air at constant pressure of air, $\alpha(z)$ is the absorption coefficient (in m^{-1}), $T(z) = e^{-\epsilon z}$ represents the total transmission of the laser energy, $n_T(z) = dn/dT \approx -10^{-6}$ K^{-1} is the change in the refractive index with respect to temperature, $v(z)$ is the wind speed in the transverse direction of the beam, and $D(z)$ is the beam diameter. In all of the above expressions, z is the distance from the beam director and is measured along the propagation path.

a. Constant Atmospheric Properties

Given a horizontal beam path from the source to the target, which is valid only if both the source and target are at equal altitudes above the sea level, the atmospheric

absorption coefficient, refractive index, and wind speed are all assumed constant along the propagation path, and thus the distortion number N_D can be approximated as

$$N_D = \frac{-4\sqrt{2}kP_{tot}\alpha n_T}{\rho_0 C_p \mathrm{v}} \int_0^{\ell} \frac{e^{-\epsilon z}}{D(z)} dz .$$

(52)

b.   Beam Diameter: $D(z)$

The beam diameter $D(z)$ along the propagation path has to be estimated in order to evaluate Equation (51). At the beam director, the laser beam is assumed to have a diameter of D_0. At the target (assumed to be at the beam waist), the beam has a time-averaged radius defined by Equation (44). Assuming that the beam propagates between these two points and the fundamental mode is roughly Gaussian, the beam diameter along the path can be estimated as

$$D(z) \approx 2w_{tot}\sqrt{1 + z^2\big/Z_{eff}^2} .$$

(53)

In (53), w_{tot} represents the laser beam spot radius at the target, z is the distance from the target and Z_{eff} is the "effective" Rayleigh range, which is defined such that $D(z = -\ell) = D_0$ [5], and visualized in Figure 14. Following this definition, the "effective" Rayleigh range can be described by

$$Z_{eff} \equiv \frac{\ell}{\sqrt{\dfrac{D_0^2}{4w_{tot}^2} - 1}} \quad \text{if} \quad D_0 \geq 2w_{tot} .$$

(54)
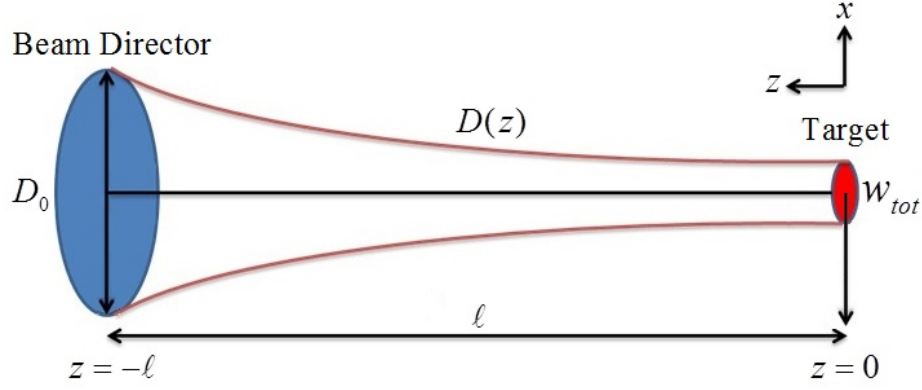
Figure 14.   Visualization of laser beam profile when $D(z=-\ell)=D_0$ and $D_0 \geq 2w_{tot}$. After [6].

However, if $D_0 < 2w_{tot}$, then the waist of the beam is located at the beam director (now at $z=0$) and the target is located at $z=\ell$, which is visualized by Figure (15). The beam diameter is then calculated as

$$D(z)=D_0\sqrt{1+z^2\big/Z_{eff}^2} \, , \tag{55}$$

where

$$Z_{eff} \equiv \frac{\ell}{\sqrt{\dfrac{4w_{tot}^2}{D_0^2}-1}} \quad \text{if} \quad D_0 < 2w_{tot}. \tag{56}$$
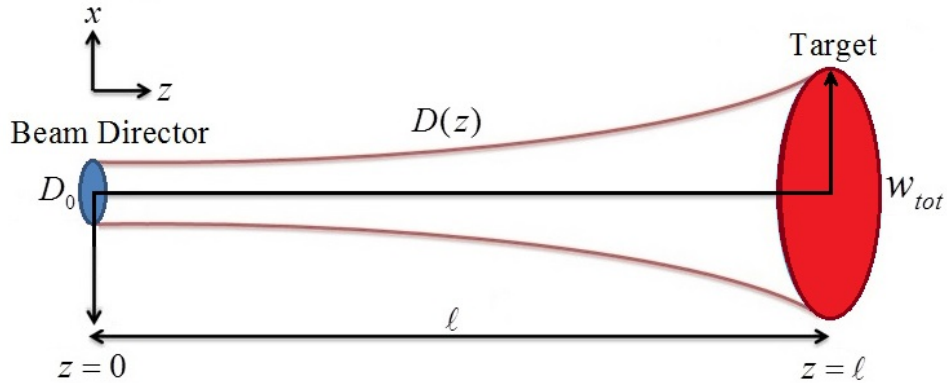
Figure 15.   Visualization of laser beam profile when target is located at $z=\ell$ and $D_0 < 2w_{tot}$, after [6].

46

2. Strehl Ratios: S_{TB}

The thermal blooming Strehl ratio S_{TB} represents a ratio of the peak irradiance of a laser beam to the peak irradiance of a reference beam where no thermal blooming has occurred. This ratio is utilized by the ANCHOR script to incorporate thermal blooming effects into the time-averaged irradiance and power-in-the-bucket calculations [29]. The Strehl ratio for a Gaussian laser beam shape can be estimated by [4]

$$S_G = \frac{1}{1+0.0625N_D^2}, \tag{57}$$

while the Strehl ratio for a uniform, or "top-hat," laser beam shape can be calculated from

$$S_U = \frac{1}{1+0.01N_D^{1.2}}, \tag{58}$$

where once more N_D represents the thermal distortion number defined by Equation (51). For the propagation simulations in this research, the beam shape described by (58) was utilized.

C.   IRRADIANCE LINEWIDTH CONVOLUTION

While Equation (43) adequately calculates time-averaged irradiance profiles for various laser beam configurations over a broad wavelength spectrum, the calculation by itself does not take into account the finite linewidth of a laser ($\sim 0.1-1.0\%$ for HELs). This characteristic is visualized in Figure 16, in which the horizontal axis represents a small portion of the electromagnetic spectrum and the vertical axis defines the strength of molecular absorption for each wavelength. The red line indicates a typical 1% HEL linewidth. As evidenced by the figure, many detailed absorption features are contained within the linewidth, and the overall on-target irradiance profile of the beam is greatly dependent on how these features affect the laser.
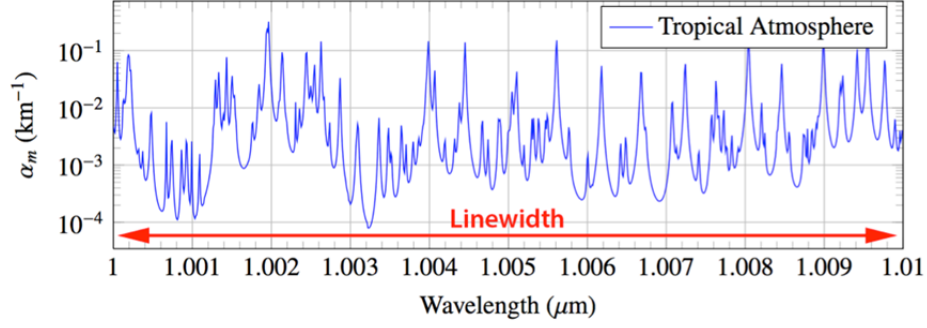
Figure 16.   Absorption features contained within a finite 1% laser linewidth. The red line indicates the spectral range of the HEL, after [26].

In order to more realistically model laser irradiance profiles, the variations in the irradiance due to the absorption features within a finite laser linewidth must be averaged. Considering a distribution of calculated irradiance profiles across a specified frequency spectrum, a typical linewidth can be described by the change in laser power as a function of the change in frequency dP/df, in which

$$\int \frac{dP}{df} df = P_{tot}.$$ (59)

Combining Equations (59) and (43), the general formula for the time-averaged irradiance for an arbitrary linewidth becomes

$$\langle I \rangle = \int \frac{dP/df}{\pi w_{tot}^2} e^{-\epsilon \ell} S_{TB} df.$$ (60)

To simplify the above equation, the assumption is made that the laser frequency spectrum has a uniform ("top-hat") distribution centered at frequency f_o and with a linewidth Δf, as shown in Figure 17. This simple top-hat approximation can be improved upon in the future, but for now adequately captures important spectral features.
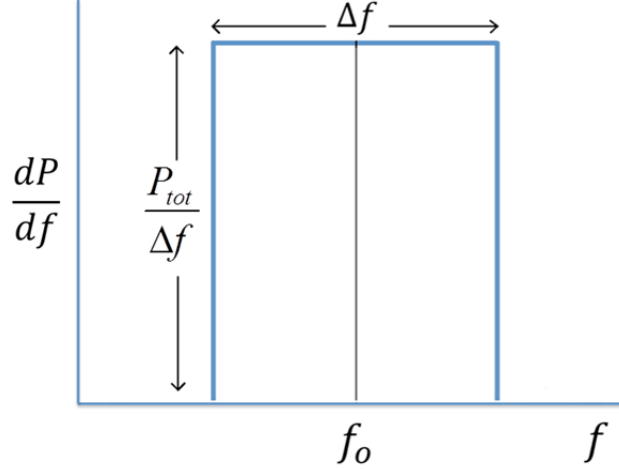
Figure 17.   Uniform distribution of a laser line centered at frequency f_o with linewidth Δf.

Following Equation (43), the time-averaged and linewidth-averaged irradiance $\langle I \rangle$ then becomes

$$\langle I \rangle = \frac{P_{tot}}{\pi \Delta f} \int\limits_{f_o - \frac{1}{2}\Delta f}^{f_o + \frac{1}{2}\Delta f} \frac{1}{w_{tot}^2} e^{-\epsilon \ell} S_{TB} \, df \; . \tag{61}$$

In implementing this calculation, which amounts to a "moving average" of irradiance values across a full frequency spectrum, Equation (61) is discretized in order to yield

$$\langle I \rangle = \frac{P_{tot}}{\pi \Delta f} \sum_{n = f_o - \frac{1}{2}\Delta f}^{f_o + \frac{1}{2}\Delta f} \frac{1}{w_{tot}^2} e^{-\epsilon \ell} S_{TB} \, \delta f \; , \tag{62}$$

where δf is the frequency difference between adjacent sampling points and $\Delta f \, / \, f$ represents the aforementioned linewidth. Typically the linewidth is $\sim 0.1-1.0\%$ for HELs.

D.   ADDITIONAL HEL PERFORMANCE METRICS

While irradiance on target is an important parameter to evaluate, it is not the only way to estimate laser performance and damage.

1. Power-in-the-bucket: P_B

Power-in-the-bucket P_B is defined as the amount of power from the HEL that falls within a pre-defined circle (the "bucket") with radius r_b on the target. Thermal blooming causes the laser beam to smear out in a complex manner, so an effective beam size $w_{tot,eff}$ is estimated as

$$\frac{1}{w_{tot,eff}^2} = \frac{S_{TB}}{w_{tot}^2},$$ (63)

where w_{tot}^2 is determined from linear effects. The irradiance can then be written as

$$\langle I \rangle = \frac{P_{tot}}{\pi w_{tot,eff}^2} e^{-\epsilon \ell}.$$ (64)

If $r_b > w_{tot,eff}$, then the power-in-the-bucket is approximated by

$$P_B \approx \langle I \rangle \left(\pi w_{tot,eff}^2 \right) = P_{tot} e^{-\epsilon \ell},$$ (65)

which is to say that all the power reaching the target plane falls within the bucket. If $r_b < w_{tot,eff}$, the power-in-the-bucket can be simply approximated by

$$P_B \approx \langle I \rangle \left(\pi r_b^2 \right).$$ (66)

2. Dwell Time: τ_D

A more physical parameter that can be used to evaluate laser beam performance is the dwell time τ_D for melting a through a certain amount of target material. Given an arbitrary material of a specified thickness, one could estimate the length of time necessary for a laser beam to remain on target in order to melt that given volume of the material.

a. Conductive and Radiative Power Transfer/Loss

As a laser beam dwells on a target, a certain amount of the laser's energy is lost due to energy conduction away from the target into the surrounding material. This conductive power transfer loss P_C (in W) can be quantified by [6]

$$P_C = \frac{2\pi r d \kappa (T_m - T_0)}{L}, \tag{67}$$

in which r represents the radius of the on-target laser spot (in m), d is the thickness of the material, κ is the thermal conductivity of the material, T_m represents the melting temperature of the target, T_0 represents the ambient and initial temperature, and L represents the distance through the material over which the temperature transitions from T_m to T_0. This distance depends on the material properties and the dwell time; for typical metals and dwell times of $\tau_D \sim 10$ s, $L \sim 2$ cm [6].

The second power loss mechanism is radiative power loss P_R, which occurs when the heated target area radiates as a black body. The radiative power loss can be estimated by [6]

$$P_R = \sigma \varepsilon A (T_m^4 - T_0^4), \tag{68}$$

where σ is the Stefan-Boltzmann constant ($\sim 5.670 \times 10^{-8}$ W m^{-2} K^{-4}), ε is the emissivity of the material (dimensionless), and the radiating surface area $A = 2\pi r^2$.

The total power loss P_L is thus defined as [6]

$$P_L = P_C + P_R. \tag{69}$$

In order to calculate the total power loss P_L, the spot size r must first be estimated. From Equation (63), the effective laser spot size is estimated as

$$r = w_{tot,eff} = \frac{w_{tot}}{\sqrt{S_{TB}}}. \tag{70}$$

This radius depends on the wavelength of the laser, atmospheric conditions and the platform/target geometry.

b.   Time Required to Melt the Target

Utilizing the previous computations, the usable melting power delivered to the target P_{melt} can be quantified by

$$P_{melt} = P_{tgt} - P_L, \tag{71}$$

in which P_{tgt} represents the laser power delivered to the target. Finally, if $P_{melt} > 0$, the dwell time can be quantified by [6]

$$\tau_D = \frac{Q_{req}}{P_{melt}},$$ (72)

in which Q_{req} represents the energy required to melt a given amount of the target.

The dwell time depends on the total range to the target since the melting power delivered to the target decreases as the range to the target increases. One can further infer that if the melting power delivered to the target does not overcome the power loss due to conduction, the dwell time effectively approaches infinity, in which case the laser beam will never significantly heat the target material to its melting point.

3.   Discussion

To evaluate the effectiveness of laser beam damage to a target, neither the beam irradiance nor the power-in-the-bucket can be independently considered. In fact, both are helpful to fully characterize the damage. The time-averaged irradiance provides valuable information because it quantifies the maximum intensity of a laser beam on a specified target and is irrespective of the size of the target. However, the irradiance does not indicate by itself how much power is being delivered to the target area.

Conversely, the power-in-the-bucket data provides a measure of how much power emitted by a laser beam is confined to a particular spot on a target. Because a substantial spot size on target is required in order to inflict significant damage, P_B provides valuable insight into the lethality of the laser beam. However, this metric depends on the size of the bucket selected, under consideration.

Dwell time, which depends on the material properties of the target and the melting volume needed for a kill, can provide guidance for operational procedures in various engagement scenarios. Together, all three metrics complement each other and provide a well-rounded characterization of laser performance.

E.   MODEL VALIDATION

In order to ensure that the ANCHOR code produces realistic laser propagation results, irradiance values at specific wavelengths were compared to the irradiance results obtained from Wavetrain. Wavetrain is a propagation code produced by MZA Associates Corporation based in Albuquerque, NM and Dayton, OH, and differs from the ANCHOR script as it actually simulates laser beam propagation by solving the paraxial wave equation [32]. This method is self-consistent and potentially more accurate than the scaling method used in ANCHOR, but also several orders of magnitude slower.

Wavetrain allows for irradiance calculations to be carried out in model atmospheres with thermal blooming effects turned on or off, and similar data can be obtained from the ANCHOR script. Irradiance values from Wavetrain were determined by averaging its output over many time steps after the pattern reached steady-state, which was ~ 0.1 s.

Table 5 displays ANCHOR and Wavetrain time-averaged irradiance profiles at various atmospheric turbulence values taking into account the effects of turbulence and thermal blooming for the $\lambda = 1.064$ μm wavelength, which corresponds to the standard wavelength for a SSL.

C_n^2 Value (m$^{-2/3}$)	Data Type	Wavetrain (W/m^2)	ANCHOR (W/m^2)
0	Without TB	3.6×10^8	3.6×10^8
	With TB	1.7×10^8	1.4×10^8
10^{-16}	Without TB	2.5×10^8	1.9×10^8
	With TB	1.3×10^8	8.3×10^7
10^{-15}	Without TB	6.9×10^7	2.5×10^7
	With TB	4.1×10^7	1.3×10^7
10^{-14}	Without TB	4.1×10^6	1.7×10^6
	With TB	4.9×10^6	1.2×10^6

Table 5.   Irradiance propagation data comparison for 1.064 μm laser beam.

Table 6 displays the identical parameters to Table 5, but for the $\lambda = 3.82$ μm wavelength.

C_n^2 Value (m$^{-2/3}$)	Data Type	Wavetrain (W/m^2)	ANCHOR (W/m^2)
0	Without TB	3.5×10^7	3.5×10^7
	With TB	1.9×10^7	1.9×10^7
10^{-16}	Without TB	3.4×10^7	3.4×10^7
	With TB	1.9×10^7	1.8×10^7
10^{-15}	Without TB	2.6×10^7	2.2×10^7
	With TB	1.5×10^7	1.2×10^7
10^{-14}	Without TB	6.0×10^6	3.2×10^6
	With TB	5.8×10^6	2.2×10^6

Table 6.   Irradiance propagation data comparison for 3.82 μm laser beam.

As evidenced by the compared data sets, at small turbulence levels the ANCHOR and Wavetrain results exhibit negligible deviation. As turbulence increases to $C_n^2 \approx 10^{-14}\,\text{m}^{-2/3}$, ANCHOR and Wavetrain differ by a factor of ~ two, with the irradiance predicted by ANCHOR consistently smaller between the two codes. On closer inspection, it appears ANCHOR is overestimating the degradation of intensity due to turbulence relative to Wavetrain. Even so, despite the differences that arise between the codes under these conditions, both methods predict laser irradiance values well within an order of magnitude of each other. It should be noted that Wavetrain takes ~ one minute of computation time per run; in that same time, ACHOR completes ~ 10^5 runs.

A trend in the data arises from the observation that as the strength of turbulence increases, the strength of thermal blooming decreases. This is due to turbulence in the atmosphere causing the laser beam to spread out, lowering the peak irradiance of the beam and preventing thermal blooming from taking effect.

THIS PAGE INTENTIONALLY LEFT BLANK

VI. RESULTS

The simulated laser propagation results obtained from ANCHOR were analyzed and catalogued in various plots. Due to the efficiency of the ANCHOR script, each generated data plot represents tens to hundreds of thousands of simulation runs; nearly 10 million runs in total were conducted for this thesis.

A. STANDARD MODEL PARAMETERIZATION

To effectively utilize the ANCHOR code in evaluating laser performance, standard laser and atmosphere models were chosen in order to establish a baseline performance profile for the various studies conducted. Table 7 displays the laser and target parameters that define the standard model utilized in the ANCHOR simulations.

Laser Output Power P	100 kW
Laser Wavelength λ	0.5 μm - 5 μm
Laser Linewidth $\Delta f / f$	1%
On-Target Bucket Size r_b	5 cm
Beam Quality M^2	3
Beam Diameter at Source D	0.5 m
Platform Jitter θ_{rms}	2.0×10^{-6} rad
Target Range	5000 m
Engagement Geometry	Horizontal; 10 m Above Water Surface
Adaptive Optics	None

Table 7.   Standard model laser and target parameters for ANCHOR.

Table 8 displays the atmospheric parameters that define the standard model utilized in the ANCHOR simulations.

Atmosphere Type	Tropical, 15° Latitude [MODTRAN Model #1]
Aerosol Composition	Maritime [MODTRAN Model #4]
Temperature, T_0	300 K (80° F)
Absolute Humidity	19.7 g/m^3 (80% Relative Humidity)
Meteorological Range	23 km (Clear Day)
Precipitation	No Rain
Turbulence C_n^2	$10^{-15}\,\text{m}^{-2/3}$ (Moderate)
Wind	Transverse, 10 m/s

Table 8.   Standard model atmospheric parameters for ANCHOR.

Finally, Figure 18 displays a simple visualization of the standard model target engagement scenario, in which both the laser platform and target are positioned 10 m above the water surface and are separated by a range of 5000 m. Once again, the diameter of the laser beam at the source (and thus the beam director diameter) is 0.5 m.
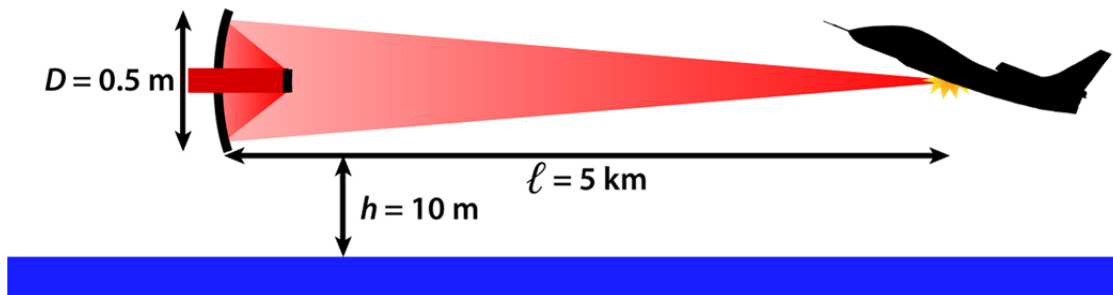

Figure 18.   Visualization of standard model target engagement scenario.

B.   STANDARD MODEL STUDIES AT 5 KM TARGET RANGE

Evaluations of the standard model were conducted by first selecting a single parameter (such as turbulence, haze, output power, etc.) and varying it over a realistic range while keeping the other parameters fixed to the standard model. The associated irradiance and power-in-the-bucket profiles were then determined for each simulation. This method allowed various known trends associated with laser propagation to be verified and visualized.

In order to ground the visualized laser performance to realistic operational requirements, a "melt threshold" is shown in the irradiance plots. This melt threshold represents the minimum on-target laser irradiance required to melt a certain volume of the target material, and is a function of the desired area to damage on the target and the laser dwell time. In this case, the target was assumed to be an arbitrary aircraft (unmanned air vehicle, helicopter, etc.) with a body comprised of 1 mm-thick aluminum. In order to attain the melt threshold, the laser must deliver enough energy to the target for the aluminum to reach its melting temperature and continue to deliver enough energy to melt through the skin, all within a 10-second laser dwell time.

Table 9 displays the various properties of aluminum necessary for determining this melt threshold.

Density ρ	2700 kg/m^3
Melting Temperature T_m	933 K
Heat Capacity C_p	897 J/kg-K
Latent Heat of Fusion H	400 kJ/kg
Thermal Conductivity κ	237 W/m-K
Emissivity ε	0.05

Table 9.   Physical properties of aluminum, from [33].

Estimating the melt threshold requires knowledge of the target material mass m and the total energy necessary to melt this mass Q_{req}, which is comprised of the energy required to reach the material's melting temperature Q_{heat} and the energy required to melt the target once the melting temperature is reached Q_{melt}. Assuming the desired region to melt is circular with a radius $r = 0.05$ m and material thickness $d = 0.001$ m, the mass m of the targeted material can be estimated by

$$m = \rho \pi r^2 d = 0.021 \text{ kg.} \tag{73}$$

Next, the energy required to heat the material is [6]

$$Q_{heat} = mC_p \left(T_m - T_0 \right) = 12.0 \text{ kJ,} \tag{74}$$

where $T_0 = 300$ K is the ambient temperature. The energy required to melt the aluminum once the melting temperature has been reached is

$$Q_{melt} = mH = 8.4 \text{ kJ.} \tag{75}$$

Finally, the total energy needed to melt is the sum of the two energy values,

$$Q_{req} = Q_{heat} + Q_{melt} = 20.4 \text{ kJ.} \tag{76}$$

With knowledge of the total energy requirement, the on-target laser irradiance required to meet the melt threshold I_{req} can be estimated by [6]

$$I_{req} = \frac{\left(\dfrac{Q_{req}}{\tau_D} + \left(P_C + P_R \right) \right)}{\pi r^2} = 0.56 \text{ MW/m}^2, \tag{77}$$

where τ_D is the laser beam dwell time (discussed in Chapter IV, Section D.2), P_C is the conductive power loss from Equation (67) and P_R is the radiative power loss from Equation (68). For the irradiance plots, the melt threshold will be identified by a solid, horizontal red line above which the laser will likely inflict significant damage to the target.

The following plots present either irradiance or power-in-the-bucket data on the vertical axis for a wavelength range of 0.5-5.0 μm, with the varying colors representing the different values of the parameter being changed. Unless otherwise stated, the laser and atmosphere parameters conform to the values listed in Tables 7 and 8.

1. Turbulence Study with a 5 km Target Range

Figure 19 displays plots of the laser irradiance for the standard model, where the C_n^2 parameter is varied from 10^{-16} m$^{-2/3}$ (weak turbulence, indicated by dark blue) to 10^{-13} m$^{-2/3}$ (strong turbulence, indicated by light blue). As evidenced by the plot, turbulence corresponding to $C_n^2 > 10^{-14}\,\mathrm{m}^{-2/3}$ may prevent a successful engagement at a 5 km range, since the irradiance generally falls near, or below, the required melt threshold to inflict significant damage to the target. Furthermore, turbulence tends to affect the shorter wavelengths more than longer wavelengths (cf. Equation 4), a trend reproduced by ANCHOR and visible in this figure.
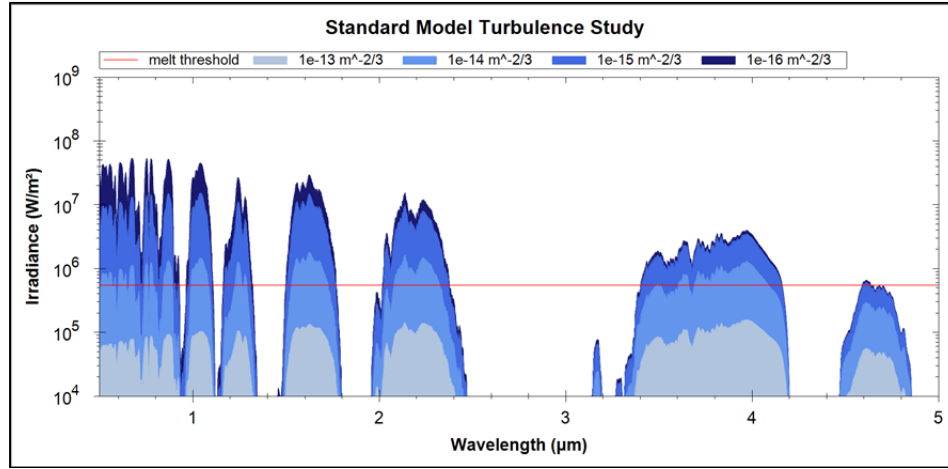

Figure 19.   Standard model turbulence study: Irradiance results indicate successful engagement at turbulences weaker than $C_n^2 = 10^{-14}\,\mathrm{m}^{-2/3}$.

Figure 20 displays plots of the power-in-the-bucket for a bucket radius of 5 cm for the same study as Figure 19. Notice that moderate turbulence $(C_n^2 = 10^{-15}\,\mathrm{m}^{-2/3})$ does not decrease power-in-the-bucket, while stronger turbulence tends to increase overall on-target laser spot size. The moderate turbulence here does not increase the spot size enough to where it falls outside the bucket, and thus all of the laser power remains confined within it. Once the turbulence reaches extreme levels, however, the on-target spot size becomes larger than the bucket size, and thus the power-in-the-bucket drops.
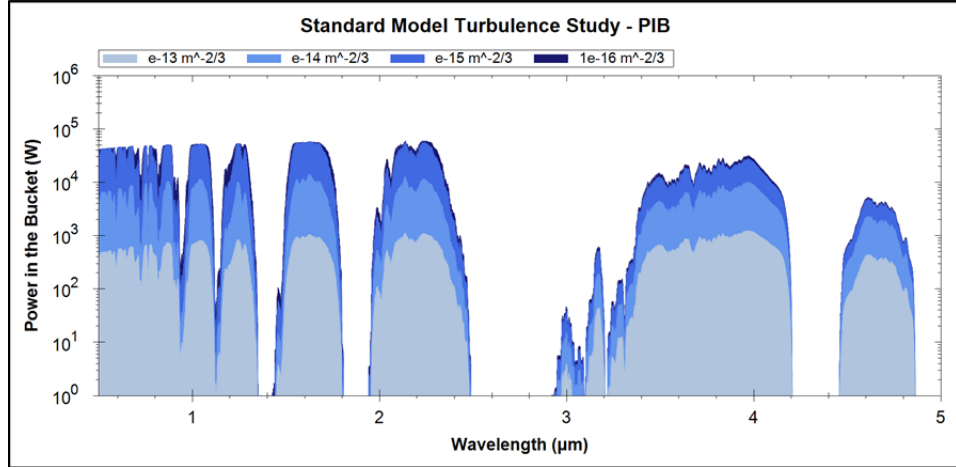
61

Figure 20.   Standard model turbulence study: Power-in-the-bucket results indicate significant loss of bucket power in the presence of strong turbulence.

2.   Variation of the Laser Beam Diameter at the Source with a 5 km Target Range

The following study examines the trends in on-target laser irradiance and power-in-the-bucket associated with varying the laser beam diameter at the source at a target range of 5 km and in the presence of weak and strong turbulence.

a.   Weak Turbulence

Figure 21 displays plots of the laser irradiance for the standard model, where the beam diameter at the source, and thus the beam director size D, has been varied from 0.3 m (light blue) to 0.7 m (dark blue) within a weak turbulence ($C_n^2 = 10^{-16} \text{m}^{-2/3}$) environment. In weak turbulence, increasing the beam director size shows marked improvement in the target irradiance. Furthermore, shorter wavelengths benefit less from the increase in the beam director size since turbulence and jitter contributions tend to dominate the time-averaged spot-size.
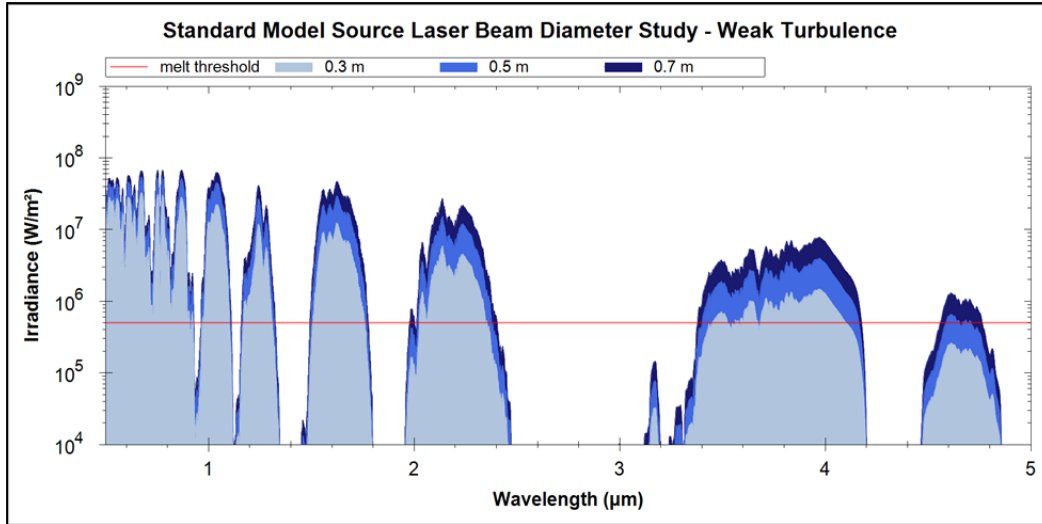
Figure 21.   Standard model weak turbulence beam director size study: Irradiance
results indicate marked improvement in laser performance by
increasing beam director size in a weakly turbulent environment.

Figure 22 represents the power-in-the-bucket results for the same study as Figure 21. Increasing the beam director size has little effect on the power-in-the-bucket in the presence of weak turbulence for shorter wavelengths; for longer wavelengths (>2 µm), the reduction of the spot size due to the larger beam director allows more of the power to be contained within the bucket.
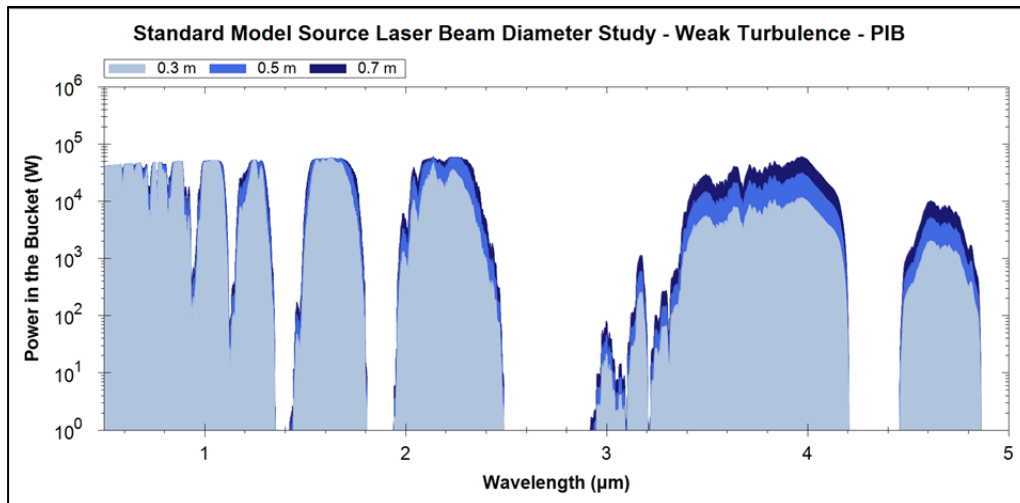

Figure 22.   Standard model weak turbulence beam director size study: Power-in-
the-bucket results indicate little effect of beam director size on power
delivered to bucket in weakly turbulent environment.

63

b. Strong Turbulence

Figure 23 displays plots of the laser irradiance for the standard model, in which the laser beam diameter at the source, and thus the beam director size D, has been varied from 0.3 m to 0.7 m within a strong turbulence ($C_n^2 = 10^{-14} \text{m}^{-2/3}$) environment. It appears that increasing the beam director size in this case has little effect on the laser performance, since the strong turbulence contribution dominates laser irradiance regardless of the size of the laser beam at the source.
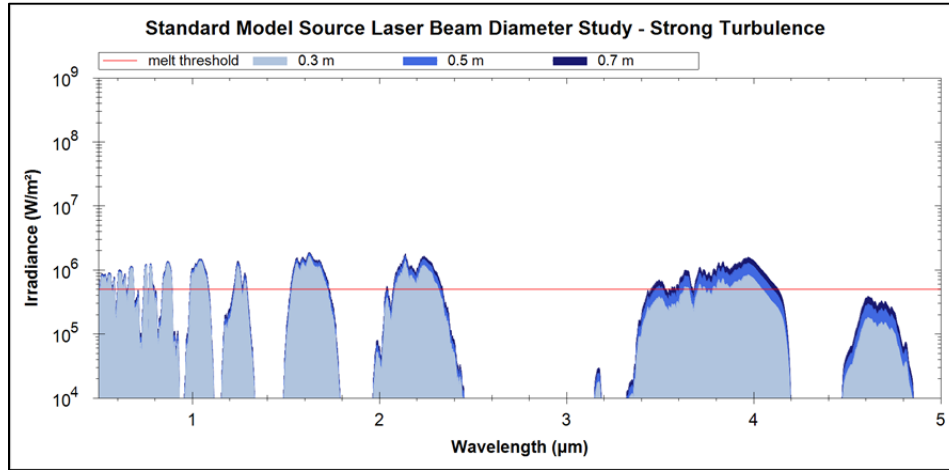

Figure 23.   Standard model strong turbulence beam director size study:
Irradiance results indicate little effect of beam director size on laser
performance in turbulent environment.

Figure 24 displays plots of the power-in-the-bucket results for the same study as Figure 23. Increasing the beam director size has once again little effect on the power delivered within the bucket on the target within a strong turbulence environment. However, in comparison to Figure 22, the bucket power has markedly dropped for all wavelength windows; this occurs because in this more turbulent environment the spot size at the target is now larger than the bucket size regardless of the wavelength.
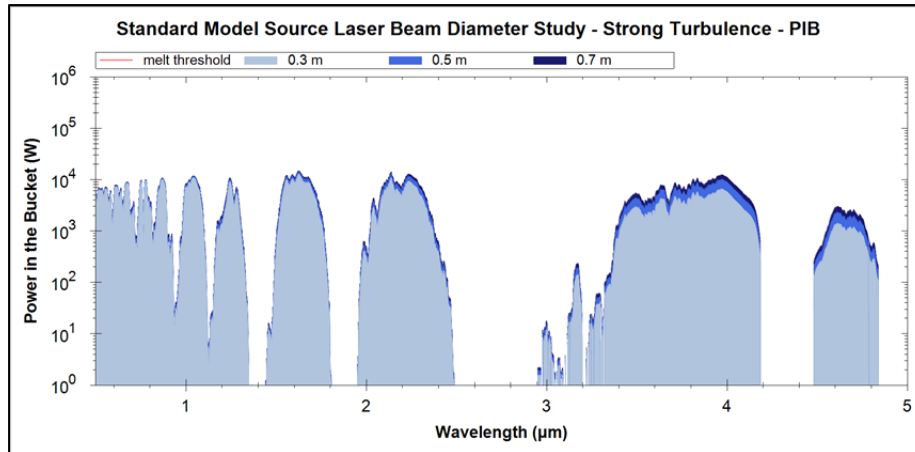
Figure 24. Standard model strong turbulence beam director size study: Power-in-the-bucket results indicate little effect from beam director size on power delivered to a bucket in a turbulent environment.

3. Meteorological Range (Haze) Study with a 5 km Target Range

Figure 25 displays plots of the laser irradiance for the standard model, where the haze (meteorological range) has been varied from 5 km visibility (hazy day, indicated by light blue) to 23 km (clear day, indicated by dark blue). Strong haze (visibility < 5 km) prevents a successful engagement at a 5 km range, as the melt threshold is not likely to be met at such limited visibility. Furthermore, haze tends to affect shorter wavelengths more than longer wavelengths. As such, wavelengths greater than 3 μm experience less of a reduction in on-target irradiance than the 0.5 μm to 2.5 μm wavelength range. This is a known trend reproduced by these results [5].
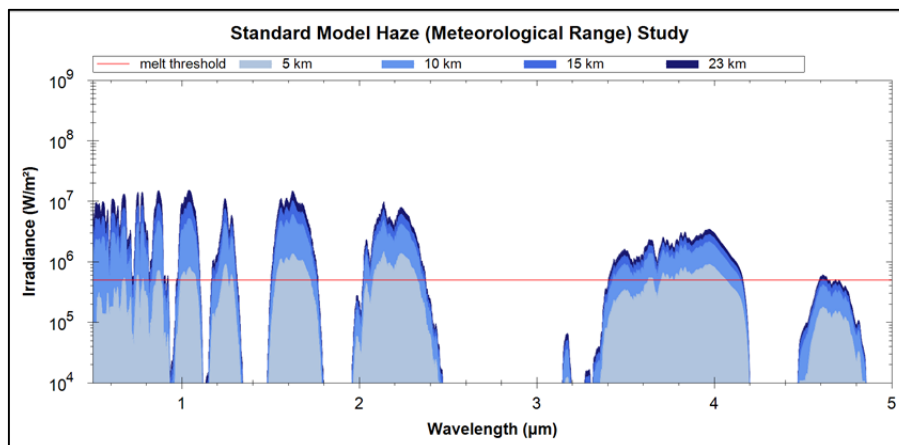

Figure 25. Standard model meteorological range study: Irradiance results indicate successful target engagement at visibilities greater than 5 km.

65

Figure 26 displays plots of the power-in-the-bucket data for the same study as Figure 25. From the data, it appears that the reduction in power-in-the-bucket is proportional to the reduction in visibility. Instead of affecting the laser spot size, like turbulence does, haze instead attenuates the laser beam as it propagates to the target via atmospheric absorption and scattering.
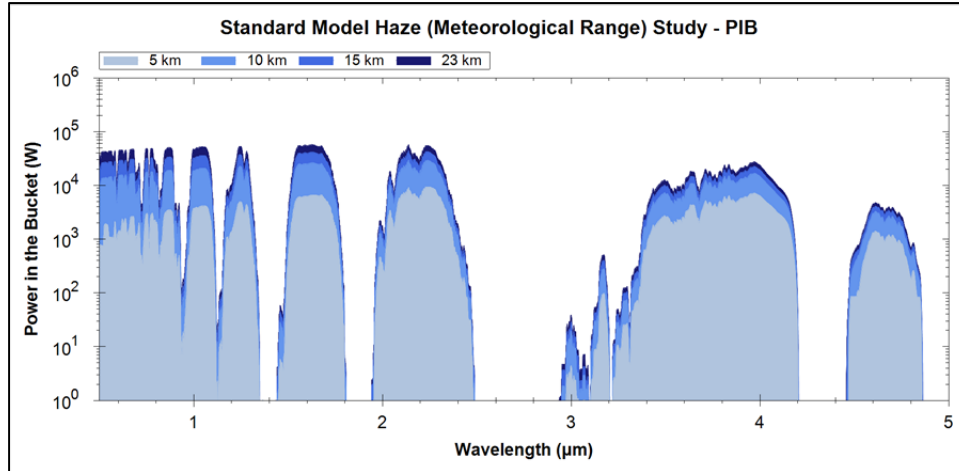

Figure 26.   Standard model meteorological range study: Power-in-the-bucket results indicate overall reduction in power due to atmospheric attenuation.

4.   Precipitation Study with a 5 km Target Range

Figure 27 displays plots of the laser irradiance for the standard model, where various amounts of precipitation have been introduced. Even the presence of light precipitation of 5.0 mm/hr rain prevents the likelihood of a successful engagement at a 5 km range due to the attenuation of the laser power by the rain droplets. Irradiance estimates in heavier precipitation rates, while successfully calculated, fall below the scale of this plot at the 5 km target range. However, engagements at shorter ranges may still be viable, as will be seen later.
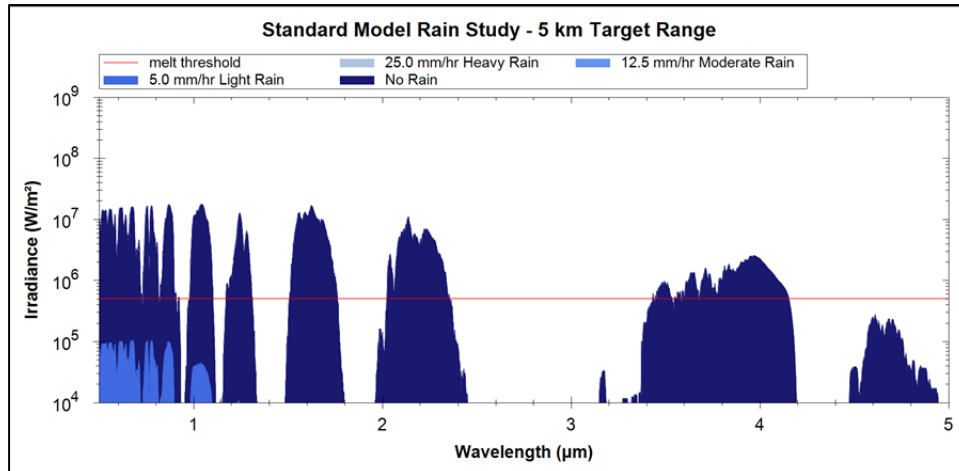
Figure 27.   Standard model precipitation study: Irradiance results indicate that even light rain prevents likelihood of a successful engagement at a 5 km target range.

Figure 28 displays plots of the power-in-the-bucket data for the same study as Figure 27. Again, the results for heavier rain rates fall below this scale shown in the plot. A successful engagement is unlikely for even the slightest amount of precipitation at a 5 km target range.

Figure 28.   Standard model precipitation study: Power-in-the-bucket results indicate significant power reduction in the presence of light rain at 5 km target range.

5.   Beam Quality Study with a 5 km Target Range

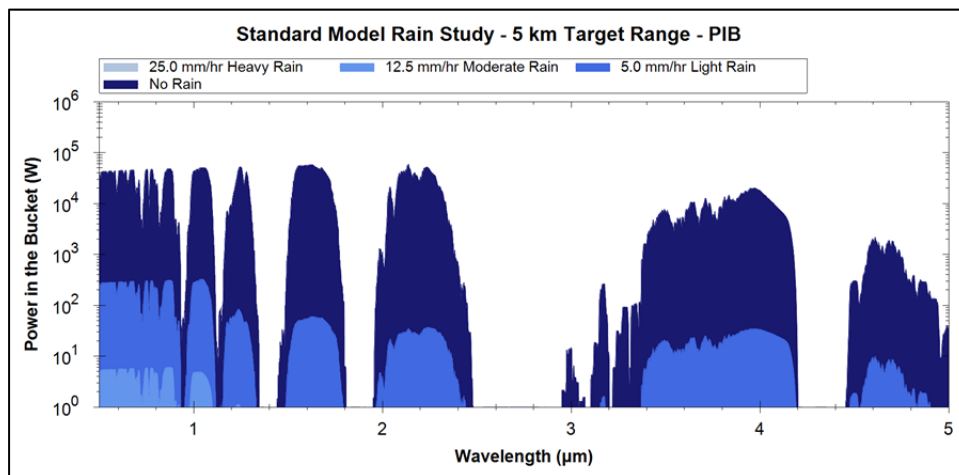Figure 29 displays plots of the laser irradiance profiles for the standard model. In this figure the beam quality factor M^2 has been varied from 1 (perfect beam quality, indicated by dark blue) to 10 (poor beam quality, indicated by light blue). Longer laser wavelengths experience a greater reduction in performance with degraded beam quality. The reason is, once again, that longer wavelength spot sizes are dominated by vacuum diffraction (cf. Equation 45), where the beam quality plays a significant role.
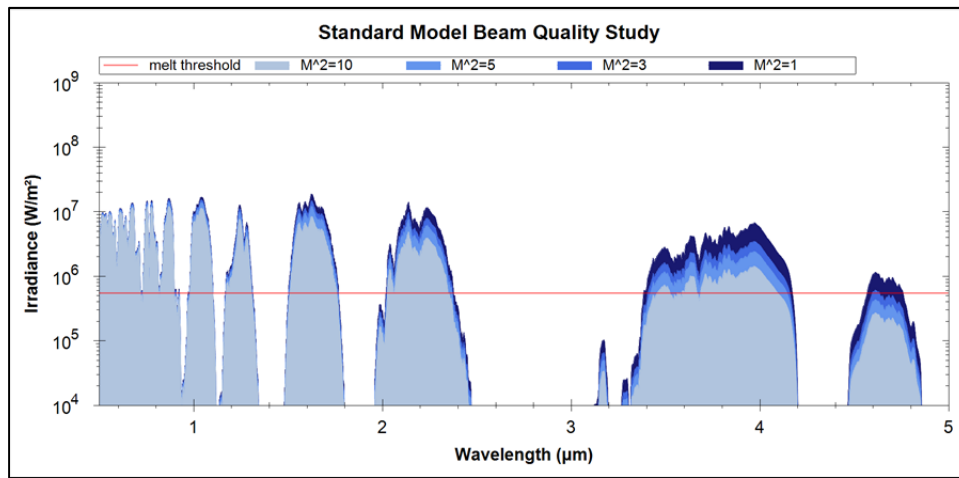
Figure 29.   Standard model beam quality study: Irradiance results indicate a greater reduction in laser performance at longer wavelengths with decreased beam quality.

Figure 30 displays plots of the power-in-the-bucket data for the same study as Figure 29. Similar to the irradiance results, degradation in the beam quality causes a reduction in power-in-the-bucket for longer laser wavelengths, again due to diffraction. The increase in spot size reaches a point to where some of the laser power falls outside the bucket, correlating to the decreased power delivered to the desired target area.
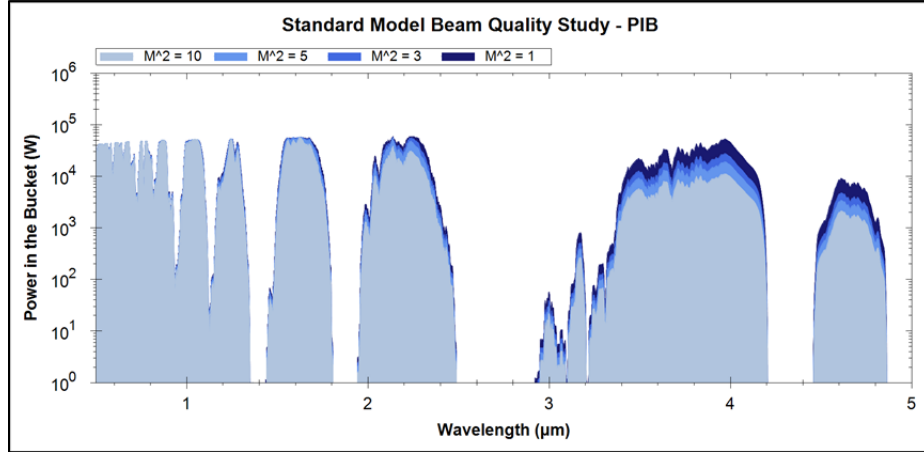
Figure 30.   Standard model beam quality study: Power-in-the-bucket results
indicate greater reduction in bucket power at longer laser wavelengths
for decreased beam quality.

6.   Platform Jitter Study with a 5 km Target Range

Figure 31 displays plots of the laser irradiance profiles for the standard model, in which the platform jitter θ_{rms} has been varied from 0 µrad (no jitter, indicated by dark blue) to 10 µrad (extreme jitter, indicated by light blue). An increase in platform jitter results in a reduction of laser performance for all wavelengths; however, shorter wavelengths tend to be affected more. While the absolute contribution of jitter to the spot size is wavelength independent (cf. Equation 50), the relative contribution is greater for shorter wavelengths (cf. Equation 44).
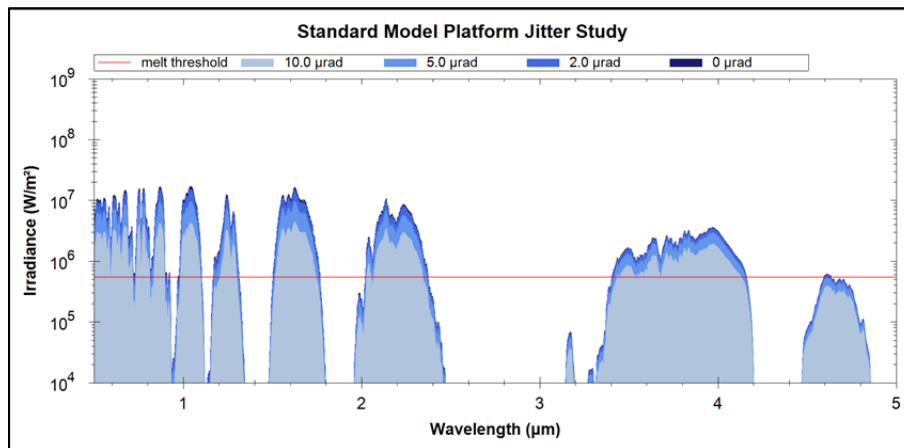

Figure 31.   Standard model platform jitter study: Irradiance results indicate an
equal reduction in laser performance with increased platform jitter for
all wavelengths, as expected.

69

Figure 32 displays plots of the power-in-the-bucket data for the same study as Figure 31. Similar to Figure 31, an increase in platform jitter increases the on-target laser spot size, which causes more laser power to fall outside the desired target area (the bucket), and thus less power is delivered within the bucket.
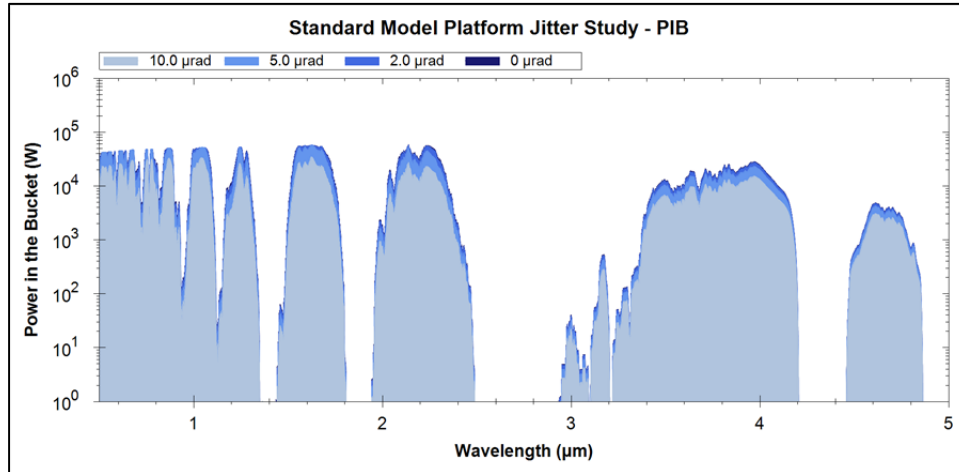
Figure 32.   Standard model platform jitter study: Power-in-the-bucket results indicate a reduction in laser performance with increased platform jitter for all wavelengths.

7.   Output Power Study with a 5 km Target Range

Figure 33 displays plots of the laser irradiance results for the standard model, in which the laser output power P has been varied from 30 kW to 200 kW. From the results, it appears that increasing laser output power from 30 kW to 100 kW results in a marked performance increase of the laser. However, doubling the output power from 100 kW to 200 kW has little benefit, as the increased laser power also increases thermal blooming, which causes a further reduction of on-axis intensity. Again, this is a known trend that is reproduced by the ANCHOR code [5].

Figure 33.   Standard model output power study: Irradiance results indicate a
marginal increase in laser performance when doubling laser output
power from 100 kW to 200 kW.

Figure 34 displays plots of the power-in-the-bucket data for the same study as Figure 33. While doubling the laser output power from 100 kW to 200 kW causes the effects of thermal blooming to be more pronounced (lowering the on-target laser intensity), power-in-the-bucket appears to be less affected by this phenomenon. While thermal blooming causes the on-target laser spot size to deform much like the depiction in Figure 6, the spot appears to remain generally confined within the desired on-target bucket, effectively delivering more power to the target at higher laser output powers and especially for shorter wavelengths.
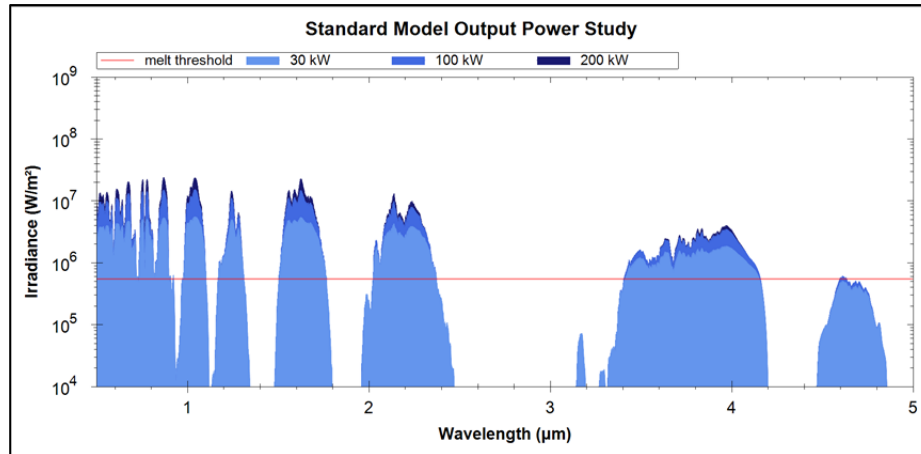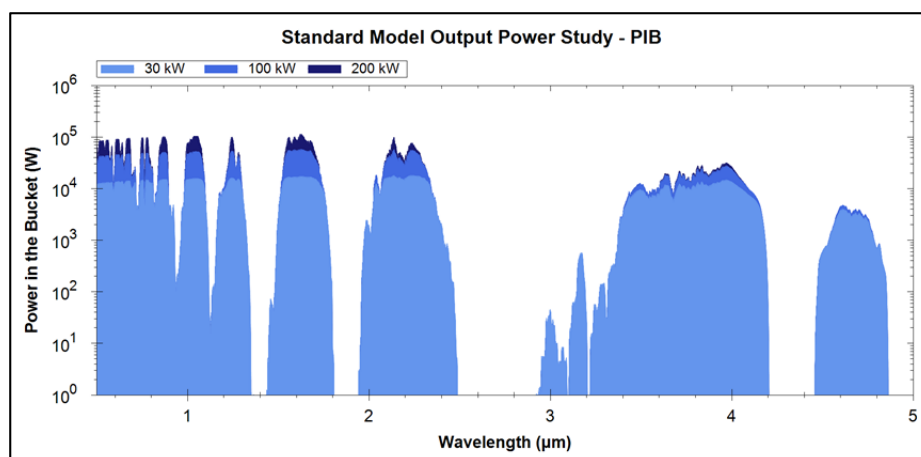

Figure 34.   Standard model output power study: Power-in-the-bucket results
indicate reasonable increase in laser performance by doubling output
power from 100 kW to 200 kW.

C.   STANDARD MODEL STUDIES AT VARIABLE TARGET RANGES

The previous studies concerned the effects of various atmospheric conditions and laser properties on overall performance while engaging a target at a fixed 5 km range. However, this approach is not wholly realistic as an adversary will rarely remain stationary in an operational environment. The following studies attempt to develop understanding of how atmospheric conditions affect laser lethality as the target closes in on the laser source.

1.   Target Range Variation Study

Figure 35 displays plots of the laser irradiance results for the standard model, in which the target range has been varied from 1000 m (indicated by dark blue) to 7000 m (indicated by light blue). It appears that on a clear day with moderate turbulence and a 10 m/s crosswind, a target is likely to be successfully engaged at ranges closer than 7000 m for systems operating at the nominal ~1 µm SSL wavelength.

Figure 35.   Standard model target range study: Irradiance results indicate likelihood of a successful engagement at ranges closer than 7 km in clear weather conditions.

Figure 36 displays plots of the power-in-the-bucket data for the same study as Figure 35. Similar to the conclusions drawn from Figure 35, as a target approaches the laser source, the laser lethality is increased. However, as the target closes in from 7000 m

to 1000 m, the power-in-the-bucket increases since less of the beam is attenuated by the atmosphere. At a range of ~1000 m, nearly all of the power from the source falls within the bucket, since the spot size is relatively small even for the longer wavelengths.
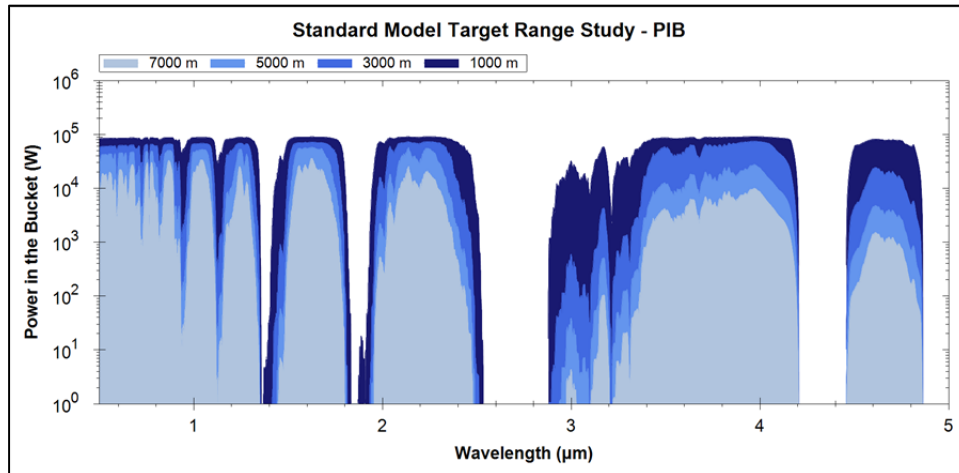
Figure 36. Standard model target range study: Power-in-the-bucket results indicate increase in laser performance as target closes in on laser source.

2. Precipitation Target Range Studies

The following irradiance and power-in-the-bucket studies evaluate laser performance at various target ranges and in the presence of precipitation of increasing severity.

a. Drizzle

Figure 37 displays plots of the laser irradiance results for the standard model in the presence of drizzle (2.5 mm/hr rain), with a variation in target proximity from 1000 m to 5000 m. While laser lethality in the presence of drizzle is marginal at best for a target range of 5 km, the on-target irradiance jumps by more than an order of magnitude as the target closes in to 3000 m, effectively making the weapon highly lethal against typical targets at this range.
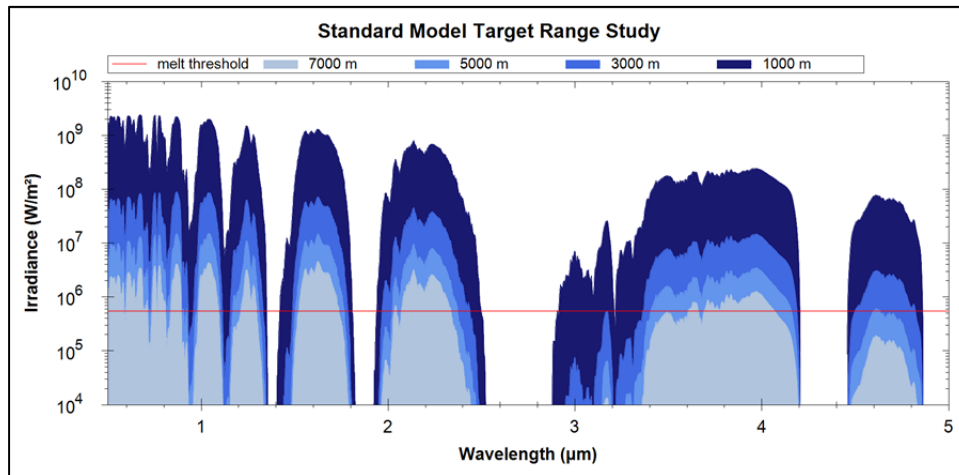
Figure 37.   Standard model drizzle target range study: Irradiance results indicate likelihood for successful engagement at ranges closer than 5 km.

Figure 38 displays plots of power-in-the-bucket results for the same study as Figure 37. Similar to the results from Figure 37, as a target approaches the laser source, the power delivered to the bucket on the adversary increases for all laser wavelengths. This increase in power-in-the-bucket, however, stems from the fact that the atmospheric precipitation attenuates laser power very effectively. The target has to be in closer proximity to the source to be hit by a substantial amount of laser power.

Figure 38.   Standard model drizzle target range study: Power-in-the-bucket results indicate marked improvement in laser performance at target ranges closer than 5 km.

b.   *Light Rain*

Figure 39 displays plots of the laser irradiance results for the standard model in the presence of light rain (5.0 mm/hr rain), with a variation in target proximity from 1000 m to 5000 m. Similar to the results for 2.5 mm/hr rain, stronger precipitation reduces the on-target laser intensity by attenuating the laser power. The target needs to be within 3000 m for the laser to effectively engage it.
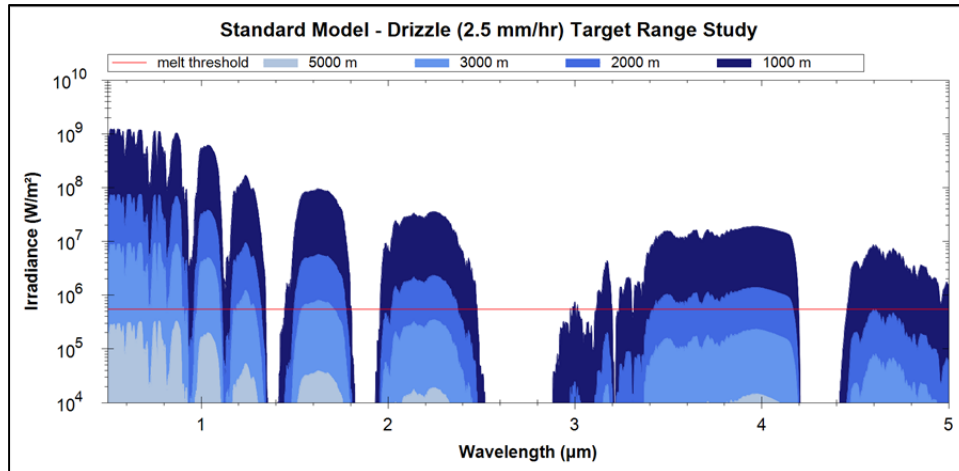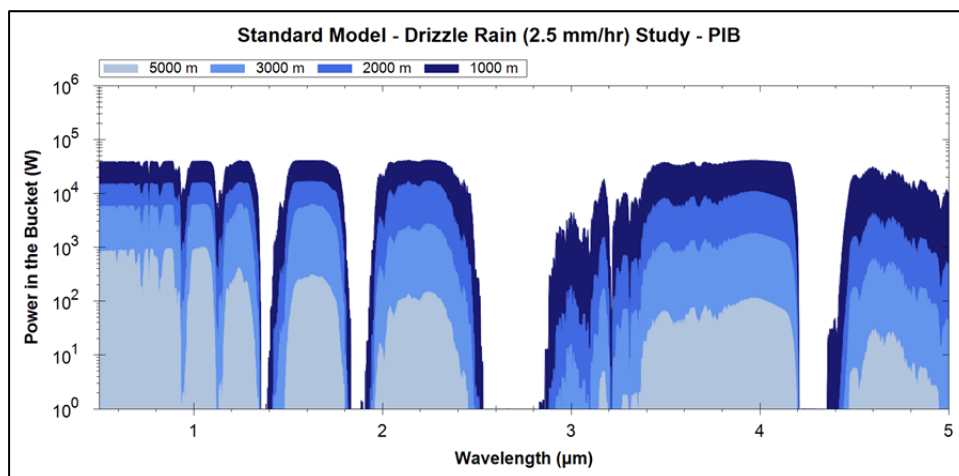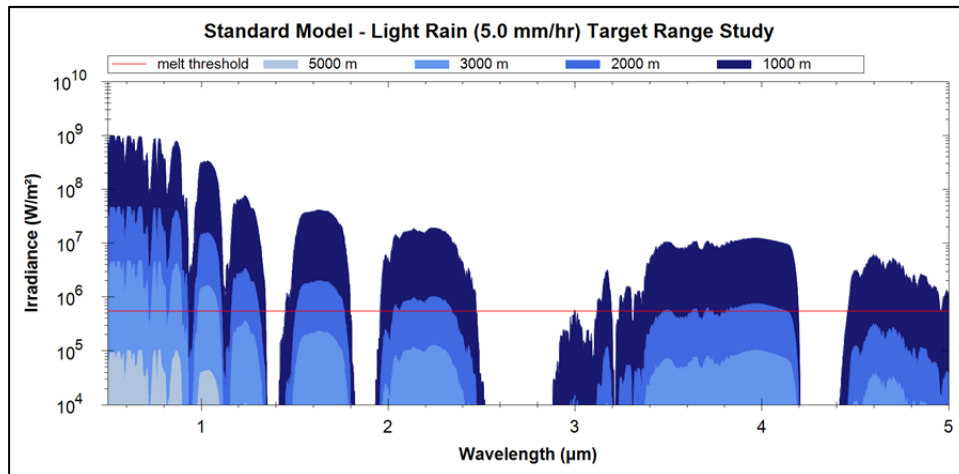

Figure 39.   Standard model light rain target range study: Irradiance results indicate likelihood of successful target engagement at ranges closer than 3 km.

Figure 40 displays plots of the power-in-the-bucket data for the same study as Figure 39. Similar to the power-in-the-bucket results for 2.5 mm/hr drizzle, a target range of less than 2000 m to the source results in an increase of power-in-the-bucket by almost an order of magnitude.

Figure 40.   Standard model light rain target range study: Power-in-the-bucket results indicate marked increase in laser performance for target ranges closer than 3 km.

c.   *Moderate Precipitation*

Figure 41 displays plots of the laser irradiance results for the standard model in the presence of moderate precipitation (12.5 mm/hr rain), in which the range to target has been varied from 1000 m to 4000 m. For shorter wavelengths the laser irradiance exceeds the melt threshold at a target range of 2 km. At a 1 km range, the on-target laser intensity exceeds the melt threshold by a large factor.

Figure 41.   Standard model moderate rain target range study: Irradiance results indicate likelihood of a successful engagement within a target range of 2 km.

Figure 42 displays plots of the power-in-the-bucket data for the same study as Figure 41. Similar to previous precipitation results, the power-in-the-bucket increases proportionally, and relatively equally for all wavelengths, to the target proximity from the source. However, the laser only truly becomes effective for target ranges closer than 2000 m.
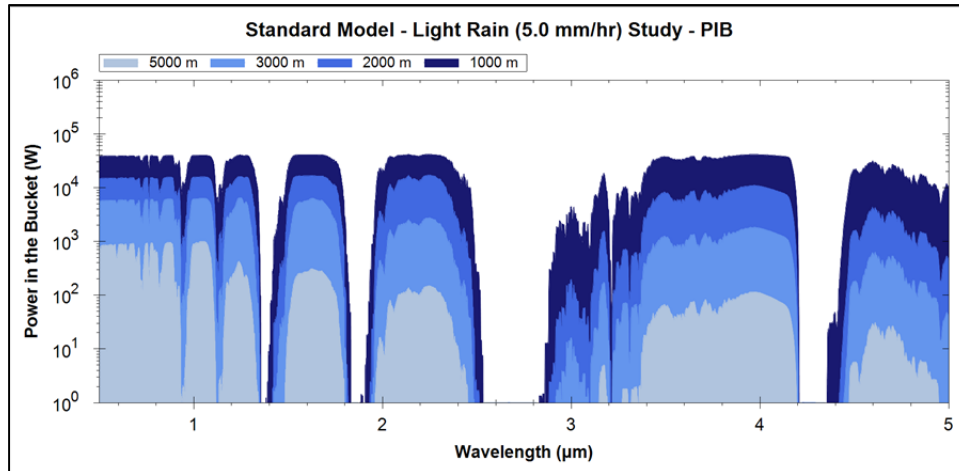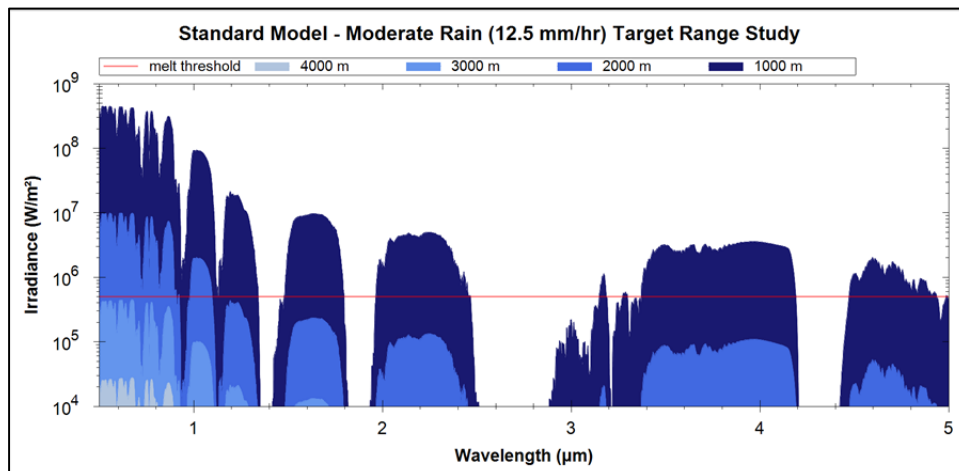

Figure 42.   Standard model moderate rain target range study: Power-in-the-bucket results indicate marked increase in laser performance for target ranges closer than 2 km.

d.   *Heavy Precipitation*

Figure 43 displays plots of the laser irradiance results for the standard model in the presence of heavy precipitation (25.0 mm/hr rain), and as the target range is varied from 1000 m to 3000 m. The on-target laser irradiance exceeds the melt threshold at a 1 km target range. Thus, even in heavy rain, a 100 kW-class HEL is a viable weapon against targets within 1000 m of the source.

Figure 43.   Standard model heavy rain target range study: Irradiance results indicate likelihood of a successful engagement at target ranges closer than 1 km.

Figure 44 displays plots of the power-in-the-bucket data for the same study as Figure 43. Similar to previous precipitation results, power-in-the-bucket increases proportionally with target proximity to the source. However, a 100 kW HEL only becomes effective as an offensive and defensive weapon in such heavy rains for target proximity of less than 1000 m. Otherwise, the actual power delivered to the target is much too low to inflict significant damage, although soft kills or blinding may still be achievable at longer ranges.
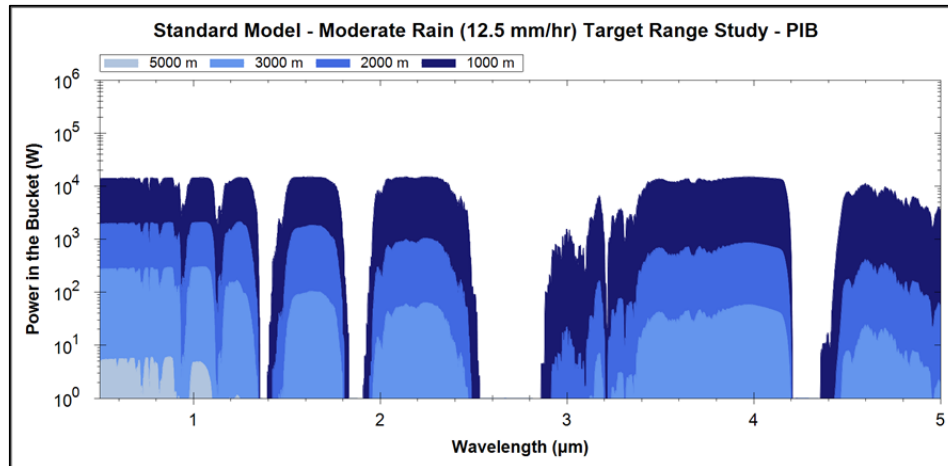

Figure 44.   Standard model heavy rain target range study: Power-in-the-bucket results increase in laser performance for target ranges closer than 1 km.

3.   Strong Haze Target Range Study

Figure 45 displays plots of the laser irradiance results for the standard model in the presence of strong haze (5 km meteorological range), within which the proximity to the target has been varied from 1000 m (indicated by dark blue) to 5000 m (indicated by light blue). In the presence of strong haze a target engagement is likely to be successful at a range of 5 km or less, as the melt threshold is exceeded at those ranges. The increase in on-target laser irradiance is dramatic; as the target approaches to within 3000 m, the laser intensity increases by more than an order of magnitude.
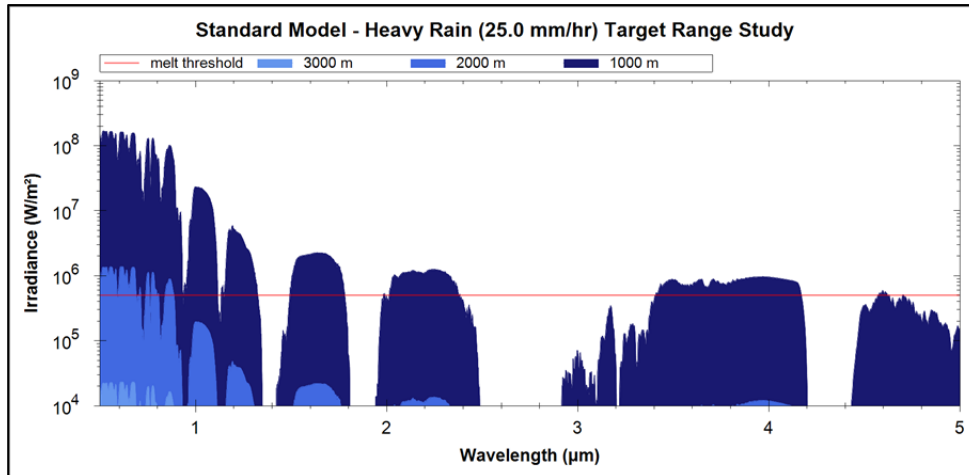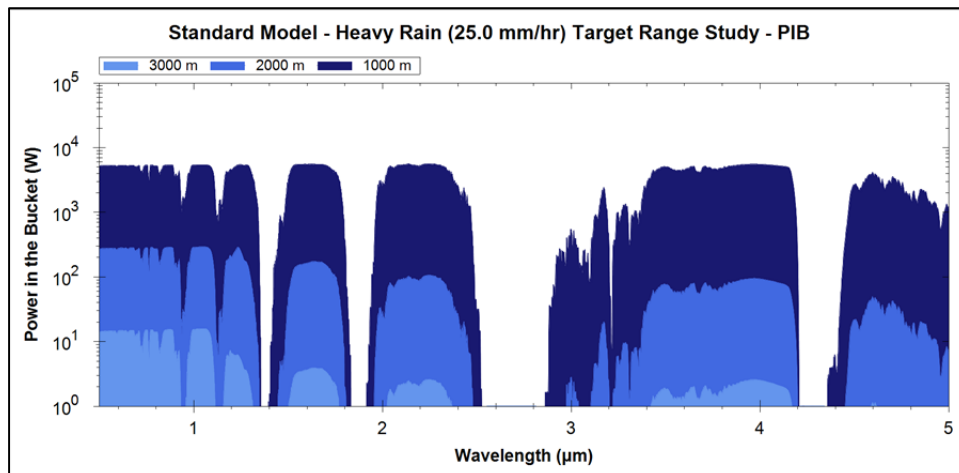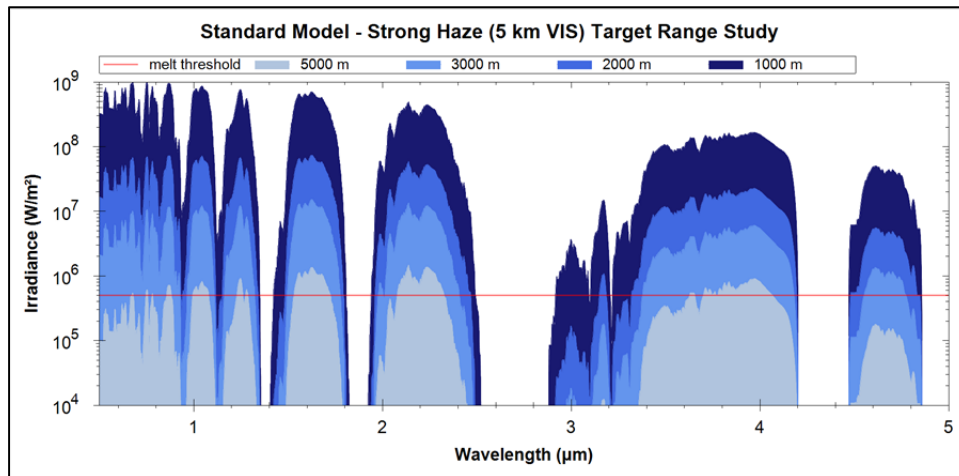

Figure 45.   Standard model strong haze target range study: Irradiance results indicate successful engagement at target ranges closer than 5 km.

Figure 46 displays plots of the power-in-the-bucket data for the same study as Figure 45. Closing the target in to the laser source results in more power delivered to the bucket. As the beam propagates a shorter distance, the hazy atmosphere attenuates the laser power less, and thus the on-target laser spot becomes more lethal.

Figure 46.   Standard model strong haze target range study: Power-in-the-bucket results indicate increase in power delivered to the target for ranges closer than 5 km.

4.   Strong Turbulence Target Range Study

Figure 47 displays plots of the laser irradiance results for the standard model in the presence of strong turbulence ($C_n^2 = 10^{-14} \, \text{m}^{-2/3}$), within which the proximity to target has been varied from 1000 m (indicated by dark blue) to 5000 m (indicated by light blue). A successful target engagement is likely for target ranges closer than 5000 m, as the melt threshold is exceeded at those ranges. Since the laser beam has to propagate a shorter distance to the target, the beam is less affected by the turbulent environment and the on-target spot size thus becomes smaller, while the laser irradiance becomes greater.

Figure 47.   Standard model strong turbulence target range study: Irradiance results indicate likelihood for successful engagement at target ranges closer than 5 km.

Figure 48 displays plots of the power-in-the-bucket data for the same study as Figure 47. It appears that as the target closes in on the position of the laser source, the power-in-the-bucket increases with the target proximity though less so at ranges closer than 2000 m. For these closer ranges, the effects of turbulence are so small that the power-in-the-bucket cannot increase with all of the available laser power already captured within it.
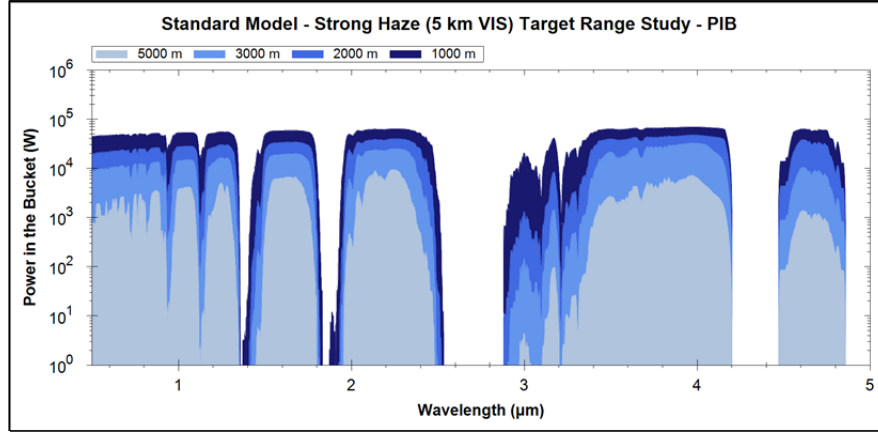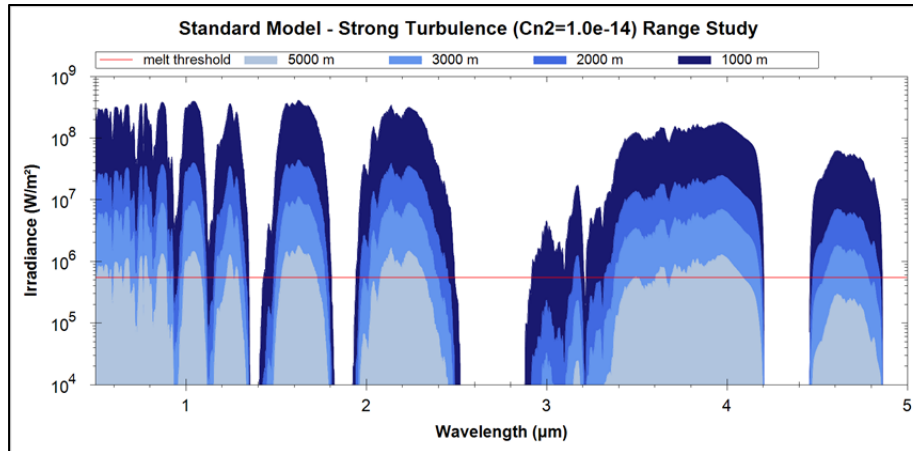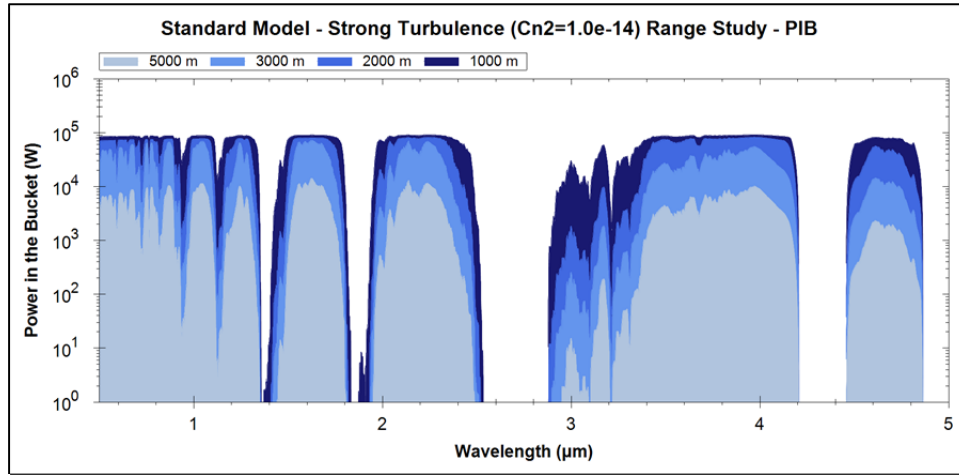

Figure 48.   Standard model strong turbulence target range study: Power-in-the-bucket results indicate increase in power delivered to target for ranges closer than 5 km.

D.   DWELL TIME STUDIES

In addition to laser irradiance and power-in-the-bucket studies, the dwell time performance metric (discussed in Chapter IV, Section D.2) was also incorporated within the standard model to give additional insight on laser performance for various weather conditions and target ranges.

1.   Example Dwell Time Calculation

Given a target with parameters as described in Section B, the required amount of time the laser spot needs to remain on target in order to inflict significant damage can be calculated by following the general procedure as discussed in Chapter IV, Section D.2. From Equation (67), the conductive power loss P_C is calculated as

$$P_C = \frac{2\pi r d\kappa \left(T_m - T_0\right)}{L} = 2.4 \text{ kW,} \tag{78}$$

and the radiative power loss P_R from Equation (68) is given as

$$P_R = \sigma \varepsilon A \left(T_m^4 - T_0^4\right) = 17 \text{ W.} \tag{79}$$

The total power loss to the surroundings is thus

$$P_C + P_R = 2.4 \text{ kW.} \tag{80}$$

In this example, the radiative power loss to the surroundings is rather negligible.

Assuming that the laser delivers 50 kW of power to the target, the available melting power is calculated as $P_{melt} = (50\text{kW} - 2.4\text{kW}) \approx 48$ kW. Further assuming that the target is sufficiently damaged once 0.1 L of its skin has been melted, the energy required to melt this volume $Q_{req} \approx 153$ kJ. Finally, the dwell time required to melt the 0.1 liters of aircraft skin can be estimated by Equation (72) as

$$\tau_D = \frac{Q_{req}}{P_{melt}} \approx 3 \text{ sec.} \tag{81}$$

Of course, the actual dwell times depend upon the specifics of the target. The following studies aim to determine the dwell times required for a laser with the attributes listed in Table 7, except with a fixed 1.064 μm wavelength, to effectively melt 0.1 liters of one millimeter-thick aluminum. The specified volume implies the assumption that the beam spot will wander while on-target in order to melt the requisite volume of material. The dwell times are determined for various haze, precipitation and turbulence conditions and at different target ranges in order to fully quantify laser lethality.

2.   Dwell Time Study for Variable Visibility Conditions

Figure 49 displays plots of the estimated dwell times required for this 1.064 μm wavelength laser to inflict damage to a target in various meteorological range conditions. As evidenced by the plot, on clear days with visibility of 23 km, the required engagement dwell times fall below five seconds with target ranges of 5 km or less. On hazy days with visibility of five km, the dwell times fall below five seconds for target ranges of one thousand meters or closer. Note that the 5 km visibility curve diverges strongly at a range

of about three kilometers while the curves corresponding to less hazy conditions do so at longer ranges. This is the result of the fact that at longer ranges, the conductive and, to a lesser extent the radiative, losses prevent the aluminum from reaching its melting point regardless of the dwell time.

Figure 49.   Laser dwell times for varying meteorological range conditions:
Results indicate reasonable engagement times for target ranges less than
5 km (dependent on visibility).

3.   Dwell Time Study for Variable Precipitation Conditions

Figure 50 displays plots of the estimated dwell times required for a laser to inflict damage to a target in various precipitation conditions. Even small amounts of precipitation greatly affect dwell times; however, target engagements within a few kilometers range remain viable. For heavy precipitation, engagements are only viable for a target range of less than one kilometer.
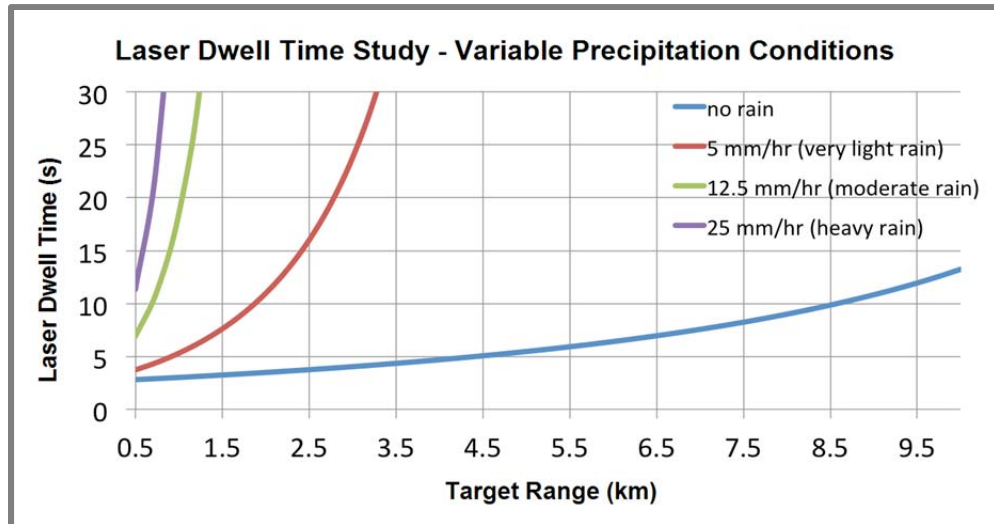
Figure 50. Laser dwell times for varying precipitation conditions: Results indicate viable engagement times in rainy conditions at target ranges less than 1 km.

4. Dwell Time Study for Variable Turbulence Conditions

Figure 51 displays plots of the estimated dwell times required for a laser to inflict damage to a target in various turbulence conditions. Dwell times remain reasonable even in a very turbulent atmosphere for target ranges of five kilometers or less.
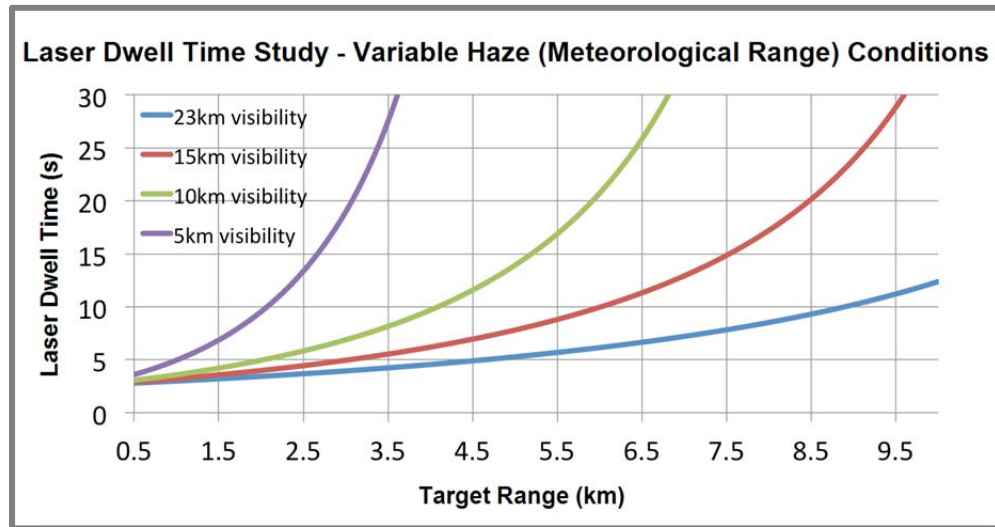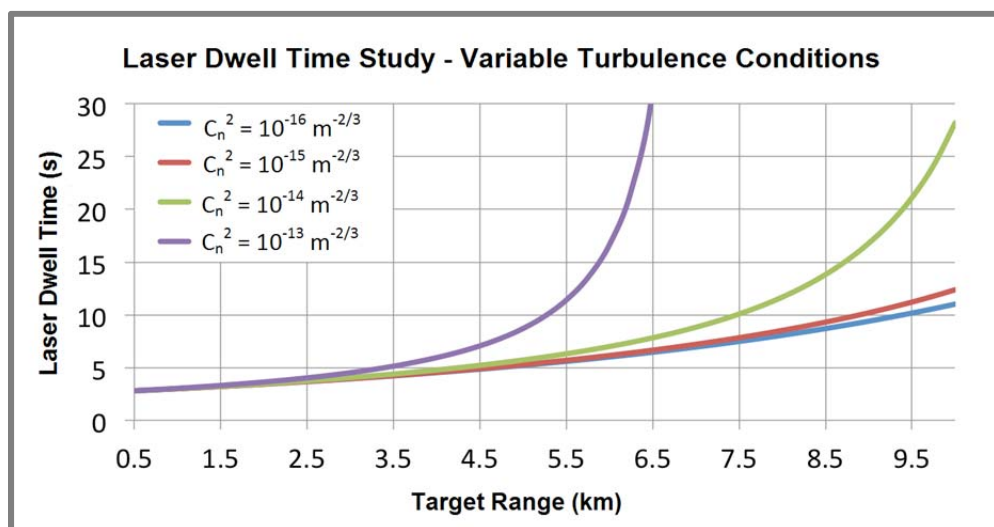

Figure 51. Laser dwell times for varying turbulence conditions: Results indicate reasonable target engagement times for ranges less than 5 km, even in the presence of turbulence.

84

VII. CONCLUSIONS

A. CONCLUSIONS FOR 5 KM TARGET RANGE

According to the results for the standard model studies at a 5 km target range, the 100 kW-class HEL is most likely to successfully engage slow-moving targets (such as light aircraft, UAVs, etc.) only in mild atmospheric conditions. Specifically, this requirement is met if atmospheric turbulence is weak to moderate ($C_n^2 = 10^{-16}\,\mathrm{m}^{-2/3}$ to $10^{-15}\,\mathrm{m}^{-2/3}$), the meteorological range is greater than 10 km visibility, and no appreciable precipitation is present.

Furthermore, it appears that large beam director sizes increase on-target laser irradiance in only weak turbulence conditions. It is quite possible that moderate to strong turbulence would be present on some days while in a maritime environment. So, laser weapon systems installed on naval vessels or aircraft could be designed in a more compact manner with smaller beam directors, since larger beam directors provide little added benefit in such conditions.

B. CONCLUSIONS FOR TARGET RANGES CLOSER THAN 5 KM

According to the results for the standard model studies at variable target ranges, the 100 kW-class HEL can be effectively utilized in an offensive and defensive capability against slow-moving targets (such as light aircraft, UAVs, etc.) in a greater variety of atmospheric conditions as the target range decreases below five kilometers. Since the various contributions to on-target laser irradiance (diffraction, jitter, turbulence, extinction and thermal blooming) are strongly dependent on target range, these contributions conspire to greatly increase laser irradiance at shorter distances.

Furthermore, these effects also aid in the total power delivered to the desired target area, the bucket. The closer a target is to the laser source, the lesser impact that atmospheric attenuation and beam dispersion have on the laser beam as it propagates to the objective. From these results, 100 kW-class HELs could be effectively employed

against targets in hazy, turbulent, and rainy conditions as long as the target is no more than three kilometers from the laser source, depending on the severity of the weather.

C. CONCLUSIONS FOR VARYING DWELL TIME STUDIES

According to the dwell time studies in clear weather, the 100 kW-class HEL can successfully engage and damage a slow-moving target from a range of five kilometers or closer within a five-second dwell time. For target ranges from 5 km to 10 km, longer laser dwell times (~ 15 seconds) are required to inflict a similar amount of damage. For target engagements at longer ranges and in poor weather conditions, required laser dwell times rise to greater than 10 seconds, and in some cases become unattainable (in the case of heavy rain, for example). However, for hazy, turbulent and rainy days, laser dwell times are still reasonable at shorter ranges (< 3 km).

LIST OF REFERENCES

[1]   R. O'Rourke, "Navy shipboard lasers for surface, air, and missile defense: Background and issues for Congress," *Congressional Research Service*, Jun. 2013.

[2]   P. A. Morrison and S. Niles. (2012, Sept.). *Solid state laser maturation program* [Online]. Available: http://www.onr.navy.mil/~/media/Files/Fact-Sheets/35/Solid-State-Laser-Technology-Maturation-Program-2012-a.ashx.

[3]   Q. Saulter. (2014). *High-energy laser* [Online]. Available: http://www.onr.navy.mil/Media-Center/Fact-Sheets/High-Energy-Laser.aspx.

[4]   G. P. Perram et al., *Introduction to Laser Weapon Systems*, 1st ed. Albuquerque, NM: Directed Energy Professional Society, 2010.

[5]   P. E. Nielsen, *Effects of Directed Energy Weapons*. Albuquerque, NM: Directed Energy Professional Society, 2009.

[6]   M. Alvarez, "Feasibility of high energy laser weapons onboard USMC attack helicopters," M.S. thesis, Physics Dept., Naval Postgraduate School, Monterey, CA, 2013.

[7]   Office of Naval Research. (2014, Apr.) *All systems go: Navy's laser weapon ready for summer deployment* [Online]. Available: http://www.navy.mil/submit/display.asp?story_id=80172.

[8]   R. P. Mansfield, "High energy solid state and free electron laser systems in tactical aviation," M.S. thesis, Physics Dept., Naval Postgraduate School, Monterey, CA, 2005.

[9]   K. N. Liou, *An Introduction to Atmospheric Radiation,* 2nd ed. San Diego, CA: Academic Press, 2002.

[10]   J. D. Schmidt, *Numerical Simulation of Optical Wave Propagation with Examples in MATLAB*. Bellingham, WA: Society of Photo-Optical Instrumentation Engineers (SPIE), 2010.

[11]   F. G. Gebhardt, "Twenty-five years of thermal blooming: An overview," *SPIE Proceedings*, vol. 1221, May 1990.

[12]   D. C. Smith, "High-power laser propagation: Thermal blooming," *IEEE*, vol. 65, no. 12, Dec. 1977.

[13]   L. Bradley and J. Herrmann, "Phase compensation for thermal blooming," *Appl. Opt.*, vol. 13, no. 2.

[14]   F. Evans. (2001, Sept.). *Absorption line physics* [Online]. Available: http://nit.colorado.edu/atoc5560/week4.pdf.

[15]   M. Somoza. (2006, Mar.). *Graphical depiction of the Morse potential with a harmonic potential for comparison* [Online]. Available: http://upload.wikimedia.org/wikipedia/commons/7/7a/Morse-potential.png.

[16]   Skbkekas. (2010, Mar.). *Plots of the density functions for several members of the Cauchy family of probability distributions* [Online]. Available: http://upload.wikimedia.org/wikipedia/commons/8/8c/Cauchy_pdf.svg.

[17]   R. Goody and Y. Yung, *Atmospheric Radiation: Theoretical Basis*, 2nd ed. New York, NY: Oxford University Press, 1995.

[18]   G. W. Petty, *A First Course in Atmospheric Radiation*, 2nd ed. Madison, WI: Sundog Publishing, 2004.

[19]   B. E. Rocher-Casterline et al., "Communication: Determination of the bond dissociation energy of the water dimer, $(H_2O)_2$, by velocity map imaging," *J. Chem. Phys.*, vol. 130, Jun. 2011.

[20]   E. J. Mlawer et al., "Collision-Induced effects and the water vapor continuum," Cambridge, MA: Atm. and Env. Res., 2003.

[21]   S. B. Carr, "The Aerosol models in MODTRAN: Incorporating selected measurements from northern Australia," Def. Sc. and Tech. Org. (DSTO), Edinburgh, S. Aust., DSTO-TR-1803, Dec. 2005.

[22]   S. W. Cheong and K. L. Woon, "Modeling of light extraction efficiency of scattering thin film using Mie scattering," *Optica Applicata*, vol. XLI, no. 1, 2011.

[23]   C. Mätzler and J. Ricka. (2009). *Radiative transfer* [Online]. Available: http://www.iapmw.unibe.ch/teaching/vorlesungen/radiative_transfer/skript/Lecture2009_9.pdf.

[24]   C. D. Cantrell, "Numerical methods for the accurate calculation of spherical bessel functions and the location of Mie resonances," Cent. for Appl. Opt., Univ. Texas, Dallas, Tech. Rep. 8, Aug. 1988.

[25]   *MODTRAN 5.3.2 User's Manual*, Spect. Sc., Inc., AFIT, Sp. Veh. Dir., Burlingham, MA, Kirtland AFB, NM, 2013.

[26]   L. S. Rothman et al., "The HITRAN2012 molecular spectroscopic database," *Journal of Quantitative Spectroscopy and Radiative Transfer*, vol. 130, Apr. 2013.

[27]   M. J. Alvorado et al., "Performance of the line-by-line radiative transfer model (LBLRTM) for temperature, water vapor, and trace gas retrievals: recent updates evaluated with IASI case studies," *Atmos. Chem. Phys.*, vol. 13, 2013.

[28]   S. T. Fiorino. (2013). *The laser environmental effects definition and reference (LEEDR)* [Online]. Available: http://www.afit.edu/CDE/page.cfm?page=329&tabname=Tab5A.

[29]   F. G. Gebhardt, "High power laser propagation," *Applied Optics*, vol. 15, no. 6, Jun. 1976.

[30]   T. S. Ross, *Laser Beam Quality Metrics*. Bellingham, WA: SPIE Press, 2013.

[31]   A. E. Siegman, "How to (maybe) measure laser beam quality," *Diode Pumped Solid State Lasers: Applications and Issues*, Stanford Univ., Oct. 1997.

[32]   S. Coy. (2013). *WaveTrain: A user-friendly wave optics propagation code* [Online]. Available: https://www.mza.com/publications/wtspiepaper.htm.

[33]   R. W. Powell et al., "Thermal conductivity of selected materials," *National Standard Reference Data Series – National Bureau of Standards*, no. 8, Nov. 1966.

THIS PAGE INTENTIONALLY LEFT BLANK

INITIAL DISTRIBUTION LIST

1.   Defense Technical Information Center
        Ft. Belvoir, Virginia

2.   Dudley Knox Library
        Naval Postgraduate School
        Monterey, California